PRELIMINARY DESIGN OF MESOSCALE TURBOCOMPRESSOR AND ROTORDYNAMICS TESTS OF ROTOR BEARING SYSTEM

By

MD SADDAM HOSSAIN

Presented to the Faculty of the Graduate School of
The University of Texas at Arlington in Partial Fulfillment
of the requirements
for the degree of

MASTER OF SCIENCE IN MECHANICAL ENGINEERING

THE UNIVERSITY OF TEXAS AT ARLINGTON

AUGUST 2011

DEDICATED TO ALMIGHTY, MY FAMILY AND FRIENDS

ACKNOWLEDGEMENTS

I would like to thank my committee chair, Dr. Daejong Kim and Dr. Donghyun Lee for their guidance and support throughout the course of this research. I would also like to thank Dr. Frank Lu and Dr. Dennis for obliging to be a part of my thesis defense committee.

I would also like to extend my appreciation to Kermit Beird and Sam Williams from the machine shop for their continuous help and support through the course of my research

I would like to give special thinks to Sherif Kerdy (PhD Student) in Texas A & M (College station) for helping me out in ICEM CFD Meshing and CFX solving in different simulation of my compressor CFD model.

My thanks also go to my colleagues at the Microturbomachinery Lab and my friends at The University of Texas at Arlington. I would also like to thank the machinists of UTA for their help in fabrication of the test rig.

May 12, 2011

ABSTRACT

PRELIMINARY DESIGN OF MESOSCALE TURBOCOMPRESSOR AND

ROTODYNAMIC TESTS OF ROTOR BEARING SYSTEM

MD SADDAM HOSSAIN, M.S.

The University of Texas at Arlington 2011

Supervising Professor: Daejong Kim

A mesoscale turbocompressor spinning above 500,000 RPM is evolutionary technology for micro turbochargers, turbo blowers, turbo compressors, micro-gas turbines, auxiliary power units, etc for automotive, aerospace, and fuel cell industries. Objectives of this work are:1) to evaluate different air foil bearings designed for the intended applications, and 2) to design & perform CFD analysis of a micro-compressor. CFD analysis of shrouded 3-D micro compressor was conducted using Ansys Bladegen as blade generation tool, ICEM CFD as mesh generation tool, and CFX as main solver for different design and off design cases and also for different number of blades. Comprehensive experimental facilities for testing the turbocompressor system have been also designed and proposed for future work.

TABLE OF CONTENTS

LIST OF ILLUSTRATIONS

Figure Page

LIST OF TABLES

NOMENCLATURE

D_1: Mean Diameter at inlet

D_2: Mean Diameter at outlet

ω: Rotational speed

l_1: Blade height at inlet

l_2: Blade height at outlet

α_1: Inlet flow angle

α_2: Exit flow angle

U_1: Circumferential velocity at inlet

A_1: Inlet stage Area:

$U_2 =$ Circumferential velocity at outlet:

A_2 =Outlet stage Area:

P_1: Inlet Pressure

P_2: Outlet Pressure

$\dot{m}$: Compressor stage mass flow

$T_0 = T_1$: Compressor inlet temperature

η: Stage efficiency

R: Gas constant

c_p : Specific heat

k : Specific heat ratio

P_a : Ambient pressure

Q : Volume flow,

$\dot{m}$: Mass flow,

ρ : Density,

C_r : So Radial Velocity,

h_1 : Enthalpy of gas at inlet

K_1 : Kinetic Energy at inlet

H_1 : Total energy at inlet

C_1 : Inlet absolute flow velocity

C_{r1} : Radial component of C_1

$C_{\theta 1}$: Tangential component of C_1

$W_{\theta 1}$: Tangential component of W_1

W_{r1} : Radial component of W_1

W_1 : Inlet Relative flow velocity

β_1 : Inlet relative flow angle (blade angle)

M_{a1} : Mach number at inlet

T_2 : Outlet Temperature

h_2 : Enthalpy of gas at outlet

K_2 : Kinetic Energy at outlet

H_2 : Total energy at outlet

C_2 : Exit absolute flow velocity

C_{r2} : Radial component of C_2

$C_{\theta 2}$: Tangential component of C_2

$W_{\theta 2}$: Tangential component of W_2

W_{r2} : Radial component of W_2

W_2 : Exit relative flow velocity

β_2 : Exit relative flow angle (blade angle)

M_{a2} : Mach number at outlet

ϕ : Stage flow coefficient

μ : Meridional velocity ratio

ν : Circumferential velocity ratio

l_{m} : Stage mechanical energy (specific mechanical energy)

P : Stage power

CHAPTER 1

INTRODUCTION

The recent study in Palm-sized mesoscale turbo machinery (100~200W) intending rotational speed towards/above 0.5 million revolution/min (RPM) have extensive potential applications in micro power generation such as air/fuel management systems for small fuel cells, turbo blowers, turbo compressors, micro-gas turbines, auxiliary power units, etc., which can be used for automotive, aerospace, fuel cell industries, propulsion engines for unmanned air vehicles, micro power generation for robots, small satellites, etc. As these mesoscale turbo-machines are operated at very high speed in most cases they favor air/gas-lubricated bearings. In this paper investigation was carried out to evaluate the performance, challenges, problems that were faced at the time of testing mesoscale air foil gas bearings in order to use these bearings in the designed turbo- compressor system. A centrifugal compressor was designed and flow analysis was also performed to find its performance at high speeds using commercial CFD package ANSYS CFX.

1.1. Mesoscale Bearing in Turbo-Machinery

Air bearings have wide range of application is microturbomachinery. The main advantage of the air bearing compare to conventional oil bearing is their better performance in high speed rotor systems requiring clean environment and maintenance-free operation. One type of air bearings is the corrugated bump foil bearing shown in Figure 1.1(a). Corrugated bump foils support the smooth top foil providing elastic cushion as well as damping to the journal shaft. The damping supplied by the bump foil is favorable to suppress sub-synchronous vibrations, and the compliant structure of the foil bearing can also accommodate rotor-bearing misalignment and remains in some extent. Tilting pad bearings shown in Figure 1.2 (b) have better rotordynamics stability than foil bearings even if they have smaller load capacity and also less debris and misalignment-

tolerance than foil bearing. In this study, three types of foil bearings were tested to measure the imbalance response at speed range of 200,000-400,000 rpm.

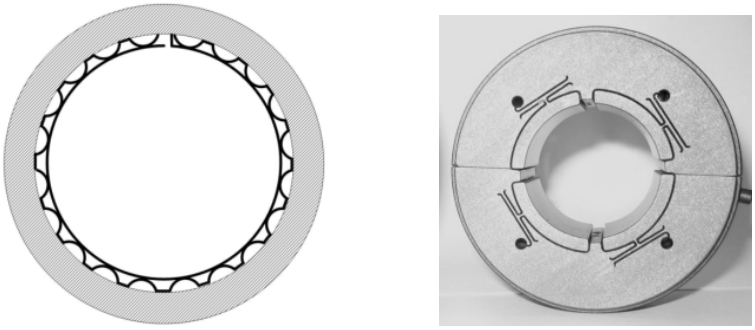

(a) (b)

Figure 1.1: Configuration of typical (a) Foil bearing and (b) Flexure pivot tilting pad bearing

1.1.1. Air Foil Bearing

In terms of tolerance to shock loads and performance etc, miniaturized foil gas bearings or tilting pad gas bearings have ultimate advantage over traditional very small ball bearings. This approach allows design of high-speed mesoscale turbomachinery with speed ranges below 1,000,000 rpm while allowing the impeller size to the level of 12mm for bearing diameter of 5mm.

In an ideal situation for high speed rigid rotors, air foil bearings (AFB) are best suited with large and uniform diameter, working below their first bending critical speed. However, air foil bearings are often considered with flexible rotors with locally large shaft diameter in regions where the bearings are located. AFBs consist of a smooth top foil and an underlying corrugated type bump foils which together act as a compliant structure. Coulomb type friction exists between the top foil and bump foil and at the same time between the bump foils and the bearing sleeve. The rotor and the bearing surface are separated by a vacant space which is termed as the nominal radial clearance of an AFB C/D ratio of about 0.0005~0.001. This clearance is necessary so as to initiate the formation of a hydrodynamic air film. Due to the viscous drag a hydrodynamic pressure is developed between the rotor and top foil i.e. in the clearance.

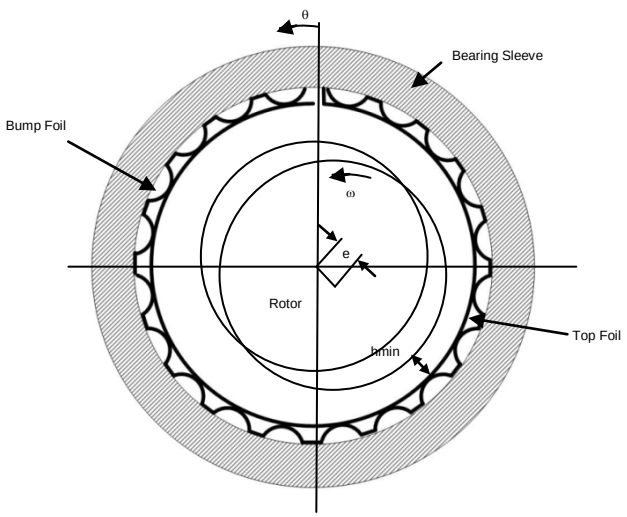

Figure 1.2: Schematic of a circular top foil, continuous bump air foil bearing showing eccentricity and radial clearance

Due to fabrication and handling difficulty of a very small element, direct miniaturizations of a mesoscale foil/tilted pad gas bearing are not simple. So for these difficulties, application of these gas bearings into small or micro-sized mesoscale turbomachinery needs moderately unusual approach in the bearing design/manufacturing. Kim et al [1, 2] introduced mesoscale foil bearings and tilting pad gas bearings manufactured through X-ray lithography and electroplating. For the foil bearings, elastic foundation was manufactured by X-ray lithography and electroplating, and they were accumulated to a bearing sleeve together with a precision-formed top foil. For the tilting pad bearing, entire bearing structure was made of electroplated Ni on polymer molds produced by X-ray lithography.

The elastic foundation for first foil bearing (Design I) shown in Figure 1.3 was adopted from [1]. This bearing was designed by Dr Daejong Kim and the manufacturing process was included X-ray lithography and electroplating. The test rig for this foil bearing which obtained from previous researchers is shown in Figure 2.2**.** Rotordynamics test of these bearing were

performed using the turbine rotor drive (Figure 2.2) up to 260.000 rpm to evaluate its imbalance response in high speed. The water fall plot for this spin test was also presented.

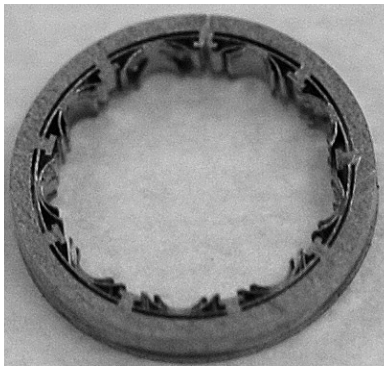

Figure 1.3: Photo of manufactured elastic foundation (Design I) using X-ray lithography and electroplating, adopted from [1]

The second foil bearing (Design 2) shown in Figure 1.4 was also designed by Dr Daejong Kim and manufactured by the previous researchers using UV and X-ray lithography, electroplating, and precision forming. Imbalance response for this bearing was evaluated by using an electric motor drive test rig. The spin tests were performed several times and water fall plots were presented.

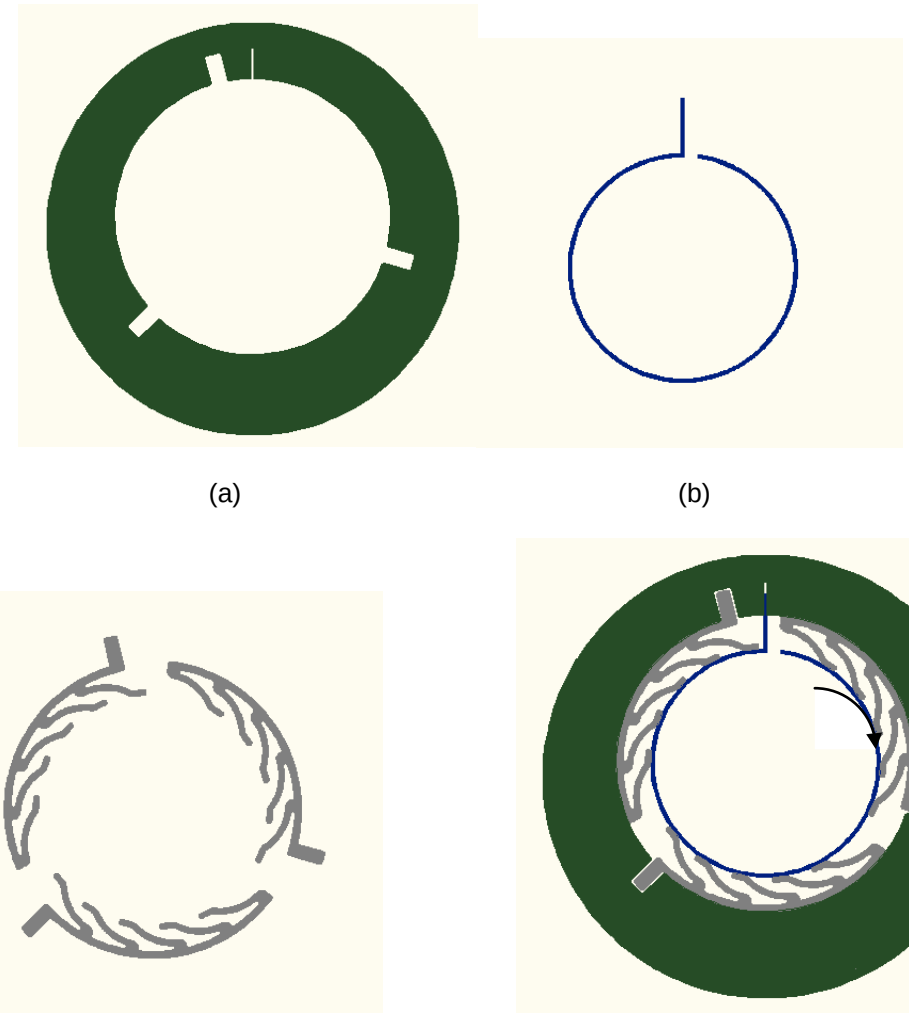

Figure 1.4: New design concept of mesoscale foil gas bearing based on two-piece sintering process of elastic foundation (Design II), (a) EDM-machined off-centered sleeve, (b) Cold-formed & age-hardened Inconel® top foil, (c) Sintered elastic foundation, (d) Assembled sub-foil bearing.

(a) (b)

Figure 1.5: Optical image of manufactured Design II elastic foundation (from X-ray lithography) and assembled foil bearing, (a) Design II elastic foundation, (b) Assembled foil bearing.

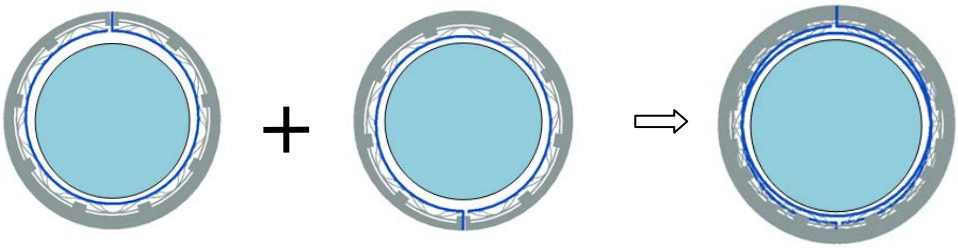

(a) + (b) → (c)

Figure 1.6: Schematic description of mesoscale foil gas bearing with a hydrodynamic preload in vertical direction; two sub-bearings are arranged as back-to-back configuration, (a) Front sub bearing, (b) Rear sub bearing, (c) One mesoscale foil bearing

Back-to-back configurations shown in Figure 1.6 of foil gas bearing that were used in spin test.

1.1.2.Turbo-Machinery

One of the widest applications of these types of gas bearings are in turbomachinery especially turbocompressor or turboblowers. This paper presents the results of the performance and operation of a centrifugal compressor at design and off design operating conditions using advanced computational fluid dynamics (CFD) techniques. ANSYS CFX is the CFD solver used

in this blind study to evaluate the ability of modern CFD software to predict the performance of centrifugal compressors operating at highly complex flows regimes.

Centrifugal compressors are essential to many mechanical systems. The focus of this thesis is on these types of machines as applied to turbocompressors or turboblowers in fuel cell, gas-turbine engines etc. This particular application places very strict requirements on weight, efficiency and operating flexibility, which has led to arguably the most advanced and high performance compressor designs. As the performance boundaries are pushed ever higher and efficiencies are further increased, the task of designing better and better compressors becomes more difficult. However some additional improvements are still possible through a better understanding of the flow behavior over the entire operational range. This can be best accomplished using high-fidelity computational fluid dynamics modeling.

Currently centrifugal compressors are designed for optimal operations at a single speed - the design speed. The design speed is usually set at the point where the compressor will operate for the longest duration, such as the cruising speed for turbo-fan aircraft engines. However, compressors must also operate at speeds other than the design point for various amounts of time. A low efficiency at these off-design points can lead to problematic engine starts and poor performance during acceleration. Furthermore, as the compressor becomes more optimized for the design speed, it is becomes increasingly likely that this effort can adversely affect its performance at off-design conditions.

The off-design cases considered included compressor operations at 60%, 70%, 85% and 100% of the on-design rotational speed (700,000 rpm). Speed lines were generated for each case and some of the cases compared to experimental measurements from the article [3]. The predicted results of those cases were found to have similar trend with the experimental measurements.

This study describes an effort to investigate and better define predicting the off-design performance of centrifugal compressors by using the capabilities of a modern CFD solver and

lead to a better understanding of the flow phenomenon. Furthermore once confidence is gained in applying CFD analysis tools to the centrifugal compressor, better compressor design that enhances off-design operation can be done and also improved performance of the compressor can be implemented.

The centrifugal compressor stage considered in this study was designed in “Ansys BladeGen”. The compressor flow geometry was modeled in TurboGrid exported from BladeGen in *.tin format, ANSYS ICEM CFD was used to generate the appropriate mesh (using Blocking technique), and ANSYS CFX was used to solve the off-design compressor flow problem. The entire ranges of off-design conditions were investigated and some of the cases were compared to experimental data [3]. Furthermore the effects of different mesh densities and different number of blade models were also examined. Finally comprehensive experimental setup for the turbocompressor system has been also designed.

1.2. Literature Review

This chapter presents a study of technical papers that served as bases for understanding of the micro turbocompressor and gas bearing technology, specifically the characteristics of foil gas bearings, and analysis methodologies. It also includes the challenges and prediction of the application of this type of bearing in micro turbomachinery, turbo compressor, turbo blowers, fuel cell application etc. Designing and experimental study of the turbocompressor consist some challenges as in the rotordynamics that is the optimized bearing and shafts system to support the turbo machines in high speed application. At high speed contact friction in ball bearing between the ball and races is so high, the temperature also goes very high and the ball typically welded between the races of the bearing. Unlike traditional Ball bearing oil free mesoscale foil bearing can support shafts in rotating machine in very high speed. At standstill, the shafts are held by a journal lining made of corrugated bump foils or elastic foundation. When the shaft starts spinning, the working fluid creates hydrodynamic pressure which lifts the foil from the shaft so there is no contact.

A useful summary outlining the recent state of foil gas bearing from the early 1970's to the late 1990's was written by [4], the developer of the second generation Compliant Air Foil Bearing. His summaries describe detail of the major development for the air foil bearings. He describes the working principle of foil bearing and states the major advantages of the foil bearing, high reliability, no scheduling maintenance, soft failure and environmentally durable. He also entails the broad application in Air Cycle Machines which is widely used in Environmental Control Units onboard aircrafts one of the primary application on that time and now a day's too.

Heshmat [5] presents a theoritical model of a bump type gas foil bearing and investigate the relationship between load, deflection, stiffness, and damping of the bump foil bearing. Friction forces are accounted for in the modeling along with localized force interaction, bump geometry, and variability of load distribution. The friction forces are considered between the bump foils and top foil as well as the bump foils and the bearing housing.

Heshmat [6] reports both speed and load performance achieving(132,000 rpm) and a load capacity of 727. N (163.6 lb) corresponding to a projected area pressure of 673.5kPa (97.68 psi) at an operating speed of 59,700 rpm). Pushing foil bearing to new level, Heshmat notes that during the testing the bearings demostrated a strong stabilizing characteristic which he attributrs to the finding from his data that confirm an increasing trend in stiffness of the foil bearing as the load increases. The maximum displacement of the shaft in his experiments is about 1mil, half of 2 mil maximum allowable value designated by the American Petroleum Institute (API) standard for the peak to peak amplitude of unfiltered vibration. Heshmat also analyzes the magnitude of the displacemet with respect to frequency.

Rubio and Andrés [7] under condition of no shaft rotation load capacity were measured of four commercial bump type foil bearings. Simple test setup was assembled to measure the foil bearing deflections resulting from static load and test was performed with three shafts of

increasing diameter to persuade a degree of preload into the foil bearing structure. Static measurement shows nonlinear deflection and the structural stiffness of the foil bearing was predicted in different shaft diameter as the foil bearing structural stiffness increases relative to the Diameter structural stiffness curve.

K. Hikichi1, S. Togo et al [8] shows the design and test results of an ultra-high speed tape type radial foil bearing for turbo machinery. Shaft with 8mm diameter and foil bearing test rig was designed based in the design methodology developed in this paper. With the foil bearing maximum rotational speed of 642 000 rpm was achieved as well as the rotor rotation was stable with moderate whirl. Test results are approximately identical in repeating start and stop cycle.

Kim and Creary [1] showes the design and manufacturing process of mesoscale (bearing diameter of 5mm) foil gas bearing used in microturbomachinery. The mesoscsale foil bearing were predicted to be stable up to the maximum simulated speed of 600,000 rpm with a self-generated preload of 0.4N to the bearing. X-ray lithigraphy and UV, electroplating and precision forming technique are used in manufacturing these bearings.

The mesoscale foil gas bearings developed By Dr. Daejong Kim [9] with a bearing diameter of 5mm,length 4mm and made of Ni was used in this study of the first rotordynamics test. The manufacturing process inculed lithography process of polymer mold, electroplating of Ni and precision forming of the top foil.

Air Foil Bearings are using in a wide variety of applications from cryogenic turbo pumps to high temperature Auxiliary Power Units for military vehicles. Foil bearings have many advantages and are more desirable due to higher efficiency, reduced noise pollution, and lower maintenance costs than oil lubricated bearings and Ball bearings.

At the time of designing foil gas bearing stiffness and damping characteristics is one of the main challenging issues as these as the key features that permits the foil bearing to posses many of its functional characteristics. Stiffness is determined by the geometry of bearing and the elastic foundation's of the material, position of the journal center with respect to the bearing center as well as spin rate, while combination of gas file compress and top foil slipping effect (coulomb friction) which also depend on spin rate, pressure field, and many other factors which also are main reason for the damping in gas bearing.

Developed for aerospace and defense applications in the 1970s, foil bearings have become the technology of choice in Air Cycle Machines (ACM), which are the heart of the environmental control system in commercial and military aircraft. These machines have demonstrated Mean Time between Failures of over 100,000 hours. Today, ACMs in almost every new environmental control system on military and commercial aircraft feature foil bearings.

Christof and Johann [10] outline a brief summary of the application areas as well as additional necessity for mega high speed drive with increases compactness. Major application lies of these mega speed drives are in dental industry, medical surgery tool, turbocompressor, turboblowers, turbochargers, fuel cell where constant air supply is required, portable gas turbine generator where rotational speed is in a order of 500,000 rpm.

Christof and Johann [11] shows experimental results and the design consideration for 100 Watt 500 000 rpm electric generator as permanent magnet electric drive and ball bearing was selected for the test rig even if foil bearing was a interested alternative for this case and considers for future investigation

Daniel and Christof et al, [12] presents a turbine driven electric generator originally was a electrically driven compressor therefore inlet guied vane has to employ and adjust for omptimum efficiency at a rated rotationl speed of 490,000 rpm. The system has been tested up to inlet air pressure of 300 KPa, maximum achieved electric power of 170 Watt and maximum measured torque was 5.2mN at 295,000 rpm.

Daniel and Christof [3, 13] present a two stage electrically driven turbocompressor has a rated speed up to 500,000 rpm, pressure ratio of 2.25 and corresponding achieved mass flow of 1g/s. A centrifugal compressor was chosen for the test as this type of compressor can create high pressure ratio but the challenge was to fabricate the compressor and fitting between the different pieces. As manufacturing tolerance increases with the downscaling consequently leakage losses are predominant for small turbomachines.

Alan H. Epstein from MIT [14, 15] present millimeter scale design using centrifugal turbine pressure ration of 2:1 to 4:1, inlet temperature was 1200K to 1600K, also reviewed the work on MEMS gas turbine engines for propulsion and power production and then present a summarized outline of appropriate MEMS fabrication techniques. It examines the microscale implications for cycle analysis, aerodynamics and structural design, amterials bearing and rotor dynamics, combustion and controls and accessories. It also discuss propulsion and power applications and brief looks at derivative technologies such as combine cycles, cogeneration, turbopumps, and rocket engines

Reza, Tousi et al [16] present 1D and 3D computational approaches for centrifugal compressor using ANSYS FLUET a commercial CFD solver and also results for two different models are compared. Meshing of the fluid region is done in Gambit using tetrahedral technique as for simulation segregated implicit solver, $k-\varepsilon$ model for turbulence, ideal gas with viscous

heating, QUICK scheme for momentum equation, SIMPLE scheme for pressure correction and 0.2 to 0.3 under relaxation factor are used. Calculation for the 1D and the 3D scheme was harmonized as it indicates the accuracy of the design and the simulation model.

Turunen and Larjola et al [17] reports the numerical results of six different vaneless diffuser construction of a centrifugal compressor where the diffuser height is narrowed 5% and 10% of its original height as the pinch made in the hub and shroud wall gives better performance for the diffuser. The larger pinch gives better performance.

Kui, Harold et al [18] shows a Computational Fluid Dynamics (CFD) model for a dual volute centrifugal compressor primarily focused on the air at impeller inlet to volute exit and the overall performance level as well as the range is also predicted.

Jun and Chuangang et al [19] present a numerical investigation of a variable inlet guide vane centrifugal compressor for different inlet angle of the guide vane and also shows the performance prediction of the compressor. Performance curve as well as the velocity vectograms shifted towards small flow domain when guide vane turns positively vice versa as simulation was done in constant speed and variable guide vane.

1.3. Research Objective

The primary goal of the present work was 1) to design a mesoscale (100-200W) turbocompressor systems which have potential applications in small fuel cells, micro/miniature power and propulsion systems for ground and aerospace applications, HVAC systems for space satalites (reverse Brayton cycles), etc. and 2) to evaluate rotor bearing performance of the simulated rotor with dummy impeller supported by air foil bearings introduced in 1.1.1.

As air foil bearing was selected for the rotor bearing system of the turbocompressor, the imbalance response of these air bearings were tested to evaluate the performance, potential problems and challenges at high speed tests. Design and CFD flow analysis of the centrifugal compressor was performed by using ANSYS CFX.

In this present work three types of air bearing were tested. Air bearing tests included imbalance response at high speed, identification of potential problems during the assembly of the bearing, and also finding the limitation for each case.

Rotordynamics test of the first Bearing (Design 1) adopted from [1] shown in Figure 1.3 were performed up to 260,000 rpm by using dental drill air turbine(Figure 2.1). The results and the water fall plot are presented.

Using metal power sintering process and also by X-ray lithography the elastic foundation was redesigned by Dr. Daejong Kim. The rotordynamics test for this type of bearing was performed with an electric motor drive (500,000 rpm max) for superior control up to 400,000 rpm. The spin test results and water fall plot are presented (up to 350,000 rpm).

The third design i.e. the foil bearing comprises with corrugated bump foil was tested with the electric motor drive and ran smoothly up to 350,000 rpm, after which the bearing started to make some weird behavior (very high synchronous and sub-synchronous vibration amplitude appeared in LabView) and finally at 410,000 rpm due to the mechanical failure of the bearing top foil the test had to be stopped. The test results are presented up to 350,000 rpm

Diffusers without any guide vane called vaneless diffuser are extensively used in industrial centrifugal compressors where a large operating range and cost-effective design are principal goal. The geometry of this kind of diffuser are very simple as two parallel plate having almost same height form a radial passage from the impeller exit to some exit radius of diffuser. A comprehensive design by using Ansys BladeGen, TurboGrid, SolidWorks and modern CFD solver was used to predict the off-design performance of a mesoscale centrifugal compressor which is presented in this paper. CFD is a powerful tool to investigate the performance and to

understand the flow behavior of the turbocompressor and has been widely used for numerical simulation in this area. A centrifugal compressor with vaneless diffuser and volute design as well as the simulation results (compressor impeller) are presented. Some experimental results from [3, 13] are shown to see the trend.

Finally, based on the experimental results of the rotordynamics performance of the current rotor-bearing system, a new rotor-bearing configuration with improved performance (in terms of manufacturing, ease of assembly, higher speeds, etc) was suggested and a new turbocompressor system with the new rotor-bearing configuration was designed.

1.4. Summary of Major Contributions

Imbalance Response of three type's air foil bearing:

Three types of mesoscale bearing provided by Dr Daejong Kim were tested to evaluate imbalance response in this study. Limitations and potential problems during the test were also investigated.

For the first air bearing shown in Figure 1.3, the test rig was designed by the previous researchers. Rotordynamics test of this bearing was performed up to 260,000 rpm. The test results are presented in this paper.

A new electric motor drive system was designed by Dr Daejong Kim and the author to forecast the rotor rotordynamics performance of the second bearing show in Figure 1.5. Spin test were executed up to 400,000 rpm and the water fall plots are presented up to 350,000 rpm.

The last foil bearing (the corrugated bump foil bearing designed/manufactured by Dr Daejong Kim) was tested up to 410,000 rpm. The spin test results up to 360,000 rpm are presented in this paper.

Finally a comprehensive turbo compressor system was designed by Dr Daejong Kim, the author and collaboration with Celeroton Inc., a company from Switzerland. Compared to the first electric motor drive in Figure 2.12 the thrust bearing assembly and the position of the journal

bearing were improved in this rotor bearing system; impeller with volute and diffuser were also included in the design.

Design and CFD simulation of a micro turbocompressor:

For design a compressor, an initial design analysis was done by calculating energy and velocity equations at both the inlet and outlet of the impeller by using excel spread sheet. After doing some calculation for combination of different mass flow, and speed we select an optimum design point maintaining Mach number below 0.85, inlet flow angle between 20-30 degree and pressure ratio of 3.0. After selecting the design point, solid modeling of this compressor was done in ANSYS BladeGen, mesh generation in ICEM-CFD and CFX was used to find performance map of this compressor and some experimental results with similar type compressor from {{440 Krähenbühl, D. 2008}} was also presented to investigate the performance of the designed compressor. CFD simulation of this micro compressor is performed in various designs and off design cases. Performance map for two different numbers of blades are shown. Surge line and chock limit for this type of compressor were also predicted.

CHAPTER 2

EXPERIMENTAL FACILITY FOR FOIL BEARING- TEST RIG PERFORMANCE

Experiment of three types of air foil bearings is done to find out the imbalance response. In order to find the imbalance response of a rotor bearing system the rotor as well as the dummy impeller should be perfectly balanced.

Air turbine (Dental Drill air turbine) was balanced at the time of purchase, so balancing of this shaft is not required. Spin test with design I (see Figure 1.3) was performed using dental drill air turbine test rig (Figure 2.1 & Figure 2.2). Test rig setup for this bearing was designed by the previous researchers.

For the electric motor drive balancing of the rotor with the dummy impeller was performed by an external balancing company. A new test rig with electric motor drive was designed and the design 2 foil bearing shown in (Figure 1.4 & Figure 1.5) and design 3(bump foil bearing in chapter 2.4) were tested using this test rig. Results of the imbalanced response were also presented.

2.1. Rotordynamic Test 1

To assess the rotordynamics performance of the bearing with Design I elastic foundations a test rig was designed. An impulse turbine collected from a local dental equipment distributer having rated speed of 300,000 rpm was assembled to a precision-machined rotor as shown in Figure 2.1. The entire rotor used in the first test was blanket-coated with 1µm thick dense Cr. As the impulse turbine was purchased as balanced condition and the shaft was precision-machined residual imbalance of assembled rotor was negligible.

Figure 2.1 Photo of a rotor with dental drill turbine before Cr coating

Test rig showing in Figure 2.2 have two fiber optic probes whice measure vibrations along the horizontal and vertical directions and for speed mesurment infrared tachmeter (max 999,999 rpm) were used. To balance out the radial force created by the air supply two opposite directions same distance from the center line were used for air injection to the turbine blade. Here two thrust pads were used to restrict the axial motion of the rotor on both sides having 5mm inner diameter with four hydrostatic air supply orifice holes with 0.25mm dia.

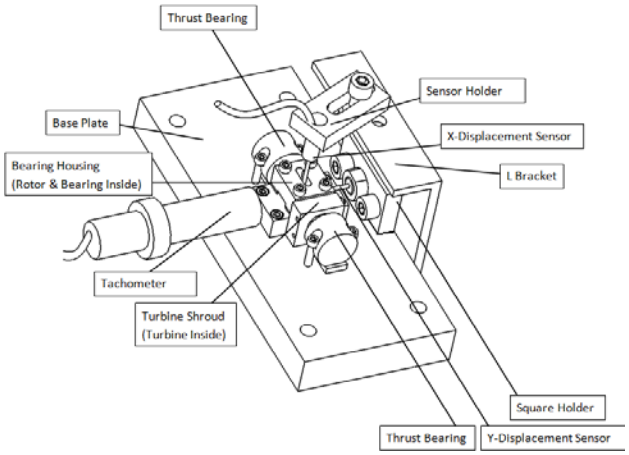

(a)

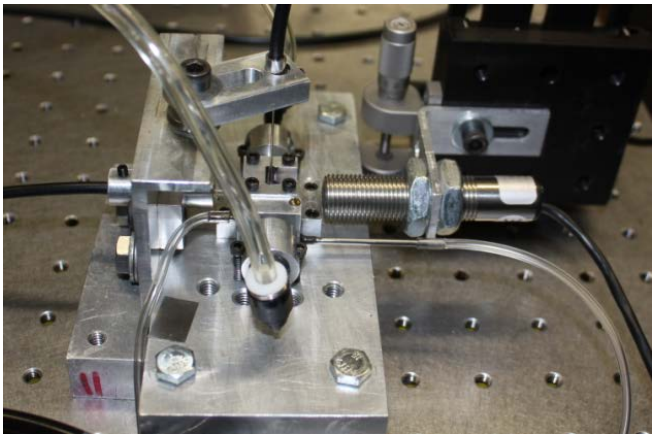

(b)

Figure 2.2: Test rig for foil bearing performance test, (a) Isometric view of the test rig, (b) Photo of test rig

Table 2.1: Bearing Parameters

Parameter	Value
Bearing radius	5 mm
Bearing Axial Length	4 mm

For calibration of the fiber optic probes micrometer-driven precision stage were used next to the Cr-coated rotor surface for precise vibration measurements. As the reflectance of the curved coated surface is different from flat smooth surface it is always necessary to do

calibrations with the target (rotor shaft) actually use in the test. For stand-off distance of the probe near-field optical range with linear displacement-output voltage region was selected. Vibration signals in both horizontal and vertical directions were measured at the rotor center plane.

In one sub bearing four layers of elastic foundations were used. To generate hydrodynamic preload in vertical direction two sub-bearings were aligned as back-to-back arrangement in Figure 1.6.

First test was with a preload in horizontal direction; the bearing in Figure 1.6(c) was rotated 90 degree in clockwise direction. Figure 2.3 are waterfall plots of signals from both horizontal and vertical direction.

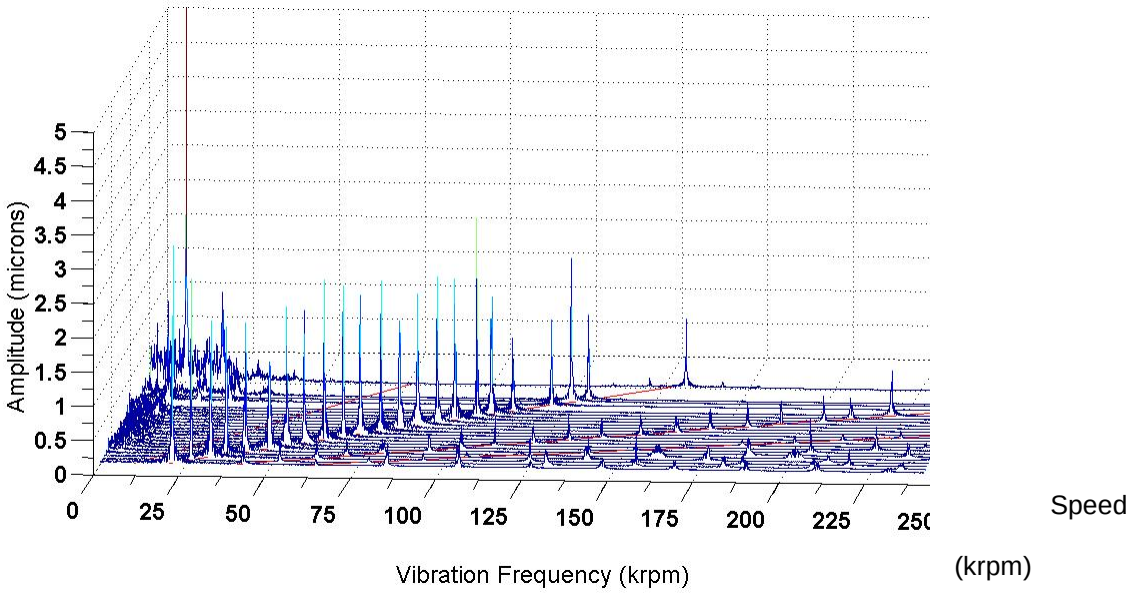

(a)

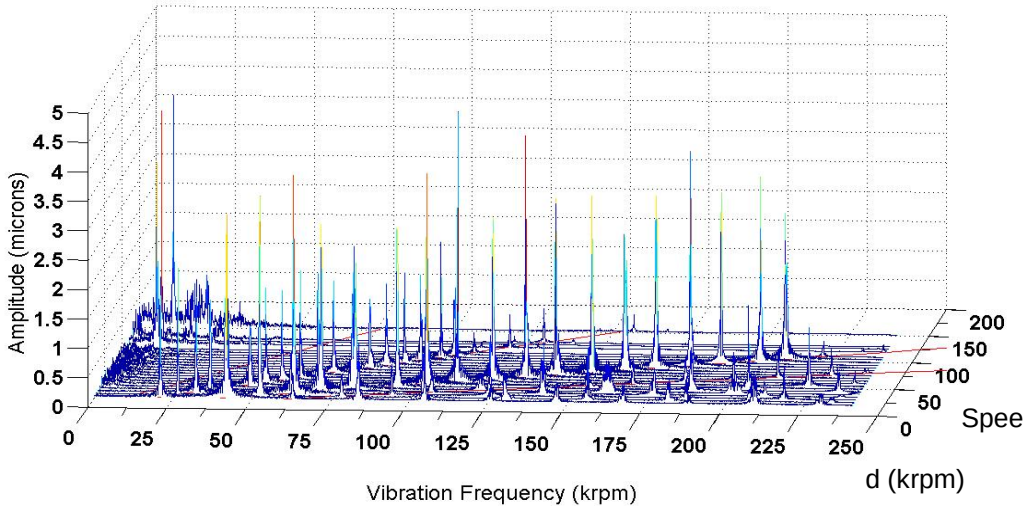

(b)

Figure 2.3: Waterfall plot from tests with preload in horizontal direction, (a) Signal from horizontal probe, (b) Signal from vertical probe.

Sub-synchronous vibrations starting to appear around 135 krpm until the rotor demonstrated steady operation up to 130 krpm. Synchronous vibration in vertical direction is higher than that in the horizontal direction as the bearing is softer in horizontal direction. There are many super synchronous vibration components bigger than the synchronous components appeared in the water fall plot although the synchronous components are smaller in horizontal direction. With the horizontal preload configuration several tests were performed but showed rather similar results with the super synchronous vibration components. Although the main cause of these strange occurrences was not well-known the author believe the non-uniform turbine tip clearance and the accurate positioning of the air nozzle may be the cause.

With bearings in vertical preload condition test rig was dismantled and assembled again (as shown in Figure 2.2) and at the same time turbine shroud was also preciously tuned to have more uniform tip clearance. The tests were performed up to 260,000 rpm (maximum speed available from 100 psi pressure source) as shown in Figure 2.6. Vibration magnitude was well-controlled within 0.5μm along both directions and no super-synchronous vibrations are observed even if lots of super-synchronous vibrations observed in Figure 2.3 After 250,000 rpm a small peak of sub-synchronous were appeared in the water fall plot.

Low efficiency of the turbine and the noise coming from the turbine in high speed affecting considerably on vibration imbalance restrict to further increase the speed. Precise speed control at high speed was very challenging because of indirect speed control by the air turbine. The turbine speeded ~40,000 rpm immediately after overcome the friction drag from the bearing. Some sub-synchronous vibration appeared at ~50,000 due to non-uniform tip clearance and strong aerodynamic force applied to turbine impeller but disappear once rotor goes to high speed.

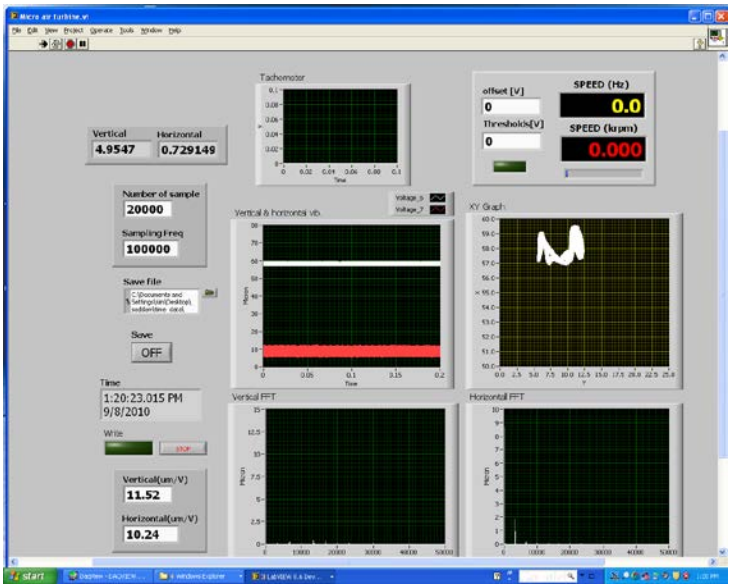

Figure 2.4: Vibration signal at 200K RPM in LabView

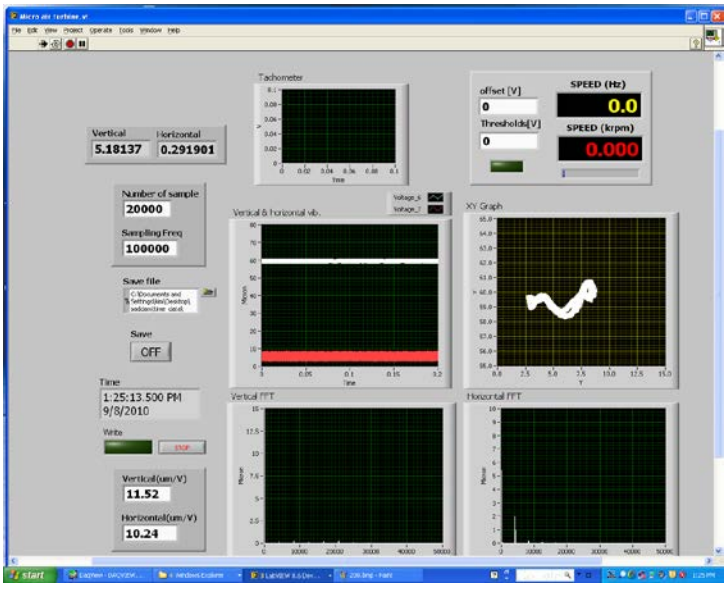

Figure 2.5: Vibration signal at 250K RPM in LabView

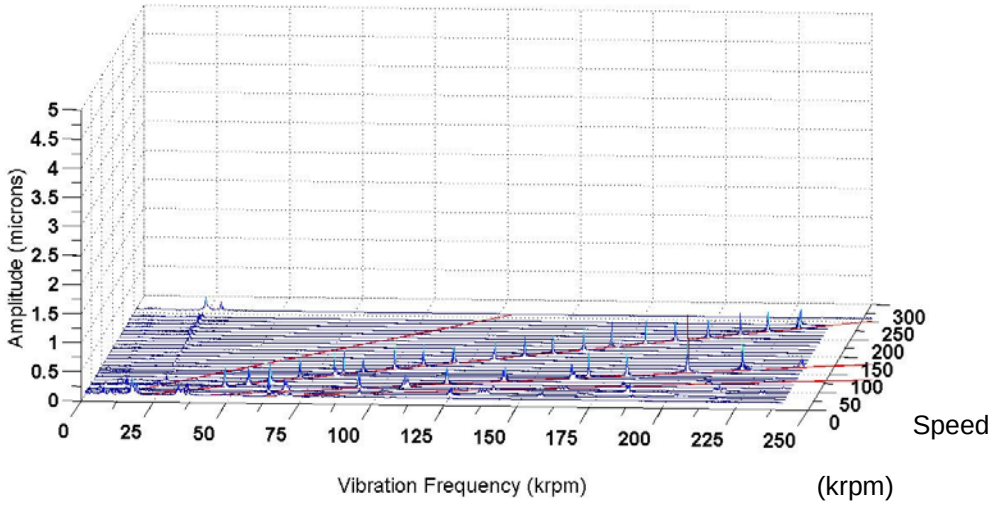

(a)

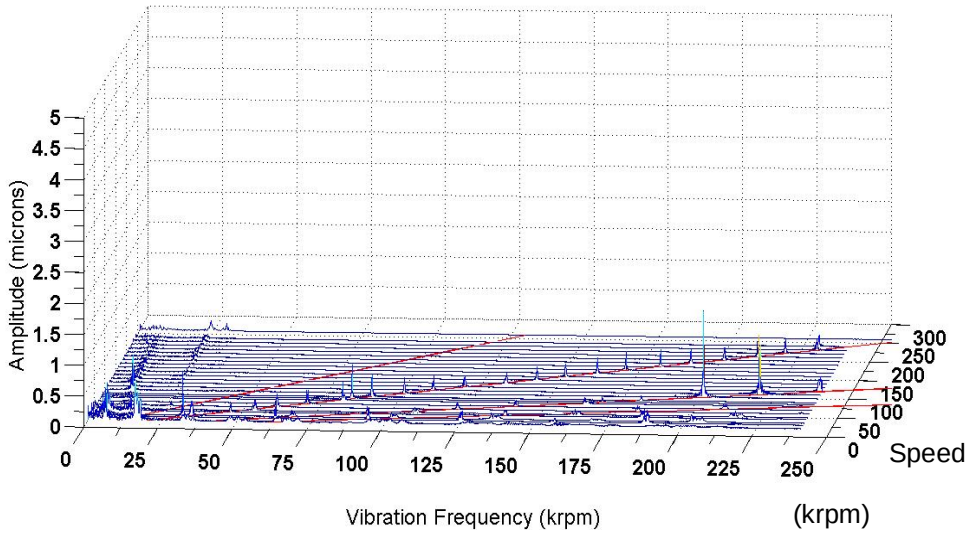

(b)

Figure 2.6: Waterfall plot from tests with preload in vertical direction. Foil bearings are from Design I elastic foundation, (a) Signal from horizontal probe, (b) Signal from vertical probe.

There are several parameters that did not have ultimate control on it. Initially the turbine shroud was installed on the base plate without any direct controlled positioned mechanism. Again at the time of disassembling and reassembling axes of the air nozzle and the center cross-section

plane of the turbine cannot be set in a same plane and at the same time distance from the center of the turbine to flow direction of the air nozzle cannot maintained exactly same which eventually resulted an unbalanced axial aerodynamic force to the rotor. Additionally, thrust pads with small outer diameter did not provide steady axial support from both sides.

2.2. Design of electric motor drive

The test rig was redesigned owing to the speed bound of the turbine drive and unmanageable turbine-rotor interaction; with an electric motor drive having small permanent magnet rotor (PM) [20] provided by Celeroton inc., Zurich, Switzerland. According to [20] the original PM rotor with two ball bearings had the first critical speed of 198,840 rpm. The rotor was redesigned (Figure 2.7 (b)) to employ both radial foil bearings and thrust air bearings, with a thrust disc having 12 mm diameter with higher bending critical speed above 1,000,000 rpm shown in Figure 2.8. A big stator housing was designed to accommodate the motor, stator and front radial foil bearing. Impeller part of the stator housing was designed to contain stator, foil bearing at impeller side and inner thrust disk as well as thrust spacer (Figure 2.9 and Figure 2.7 (a)). Motor cover at the opposite side accommodates rear foil bearing and outer thrust disk and also has the facility for cooling air injection (Figure 2.10 (a) & (b)).

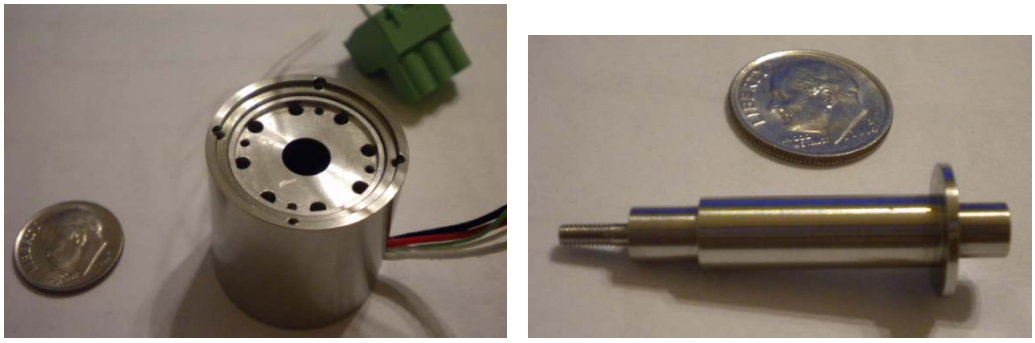

(a) (b)

Figure 2.7: Photo of micro motor drive and PM-integrated rotor, (a) Stator, (b) PM-integrated rotor.

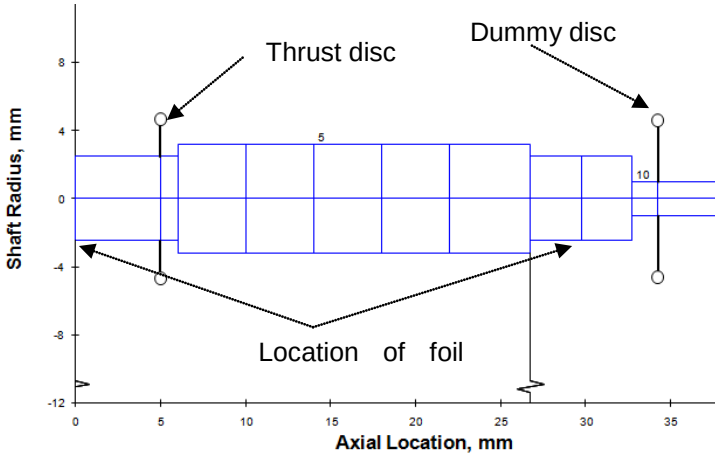

(a)

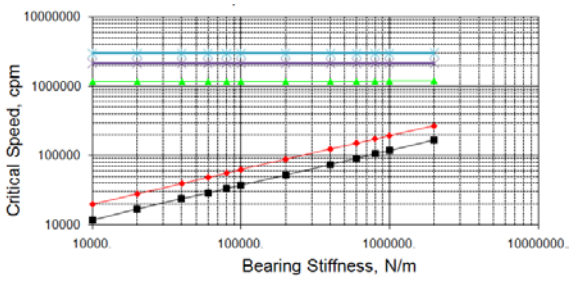

(b)

Figure 2.8 (a) Rotordynamics model and (b) Undamped critical speed map of the rotor

Figure 2.9: Photo of front air thrust bearing inside the stator housing

(a) (b)

Figure 2.10: Photo of (a) Rear air thrust bearing and (b) Rear radial foil bearing (Design II) inside the rear bearing housing

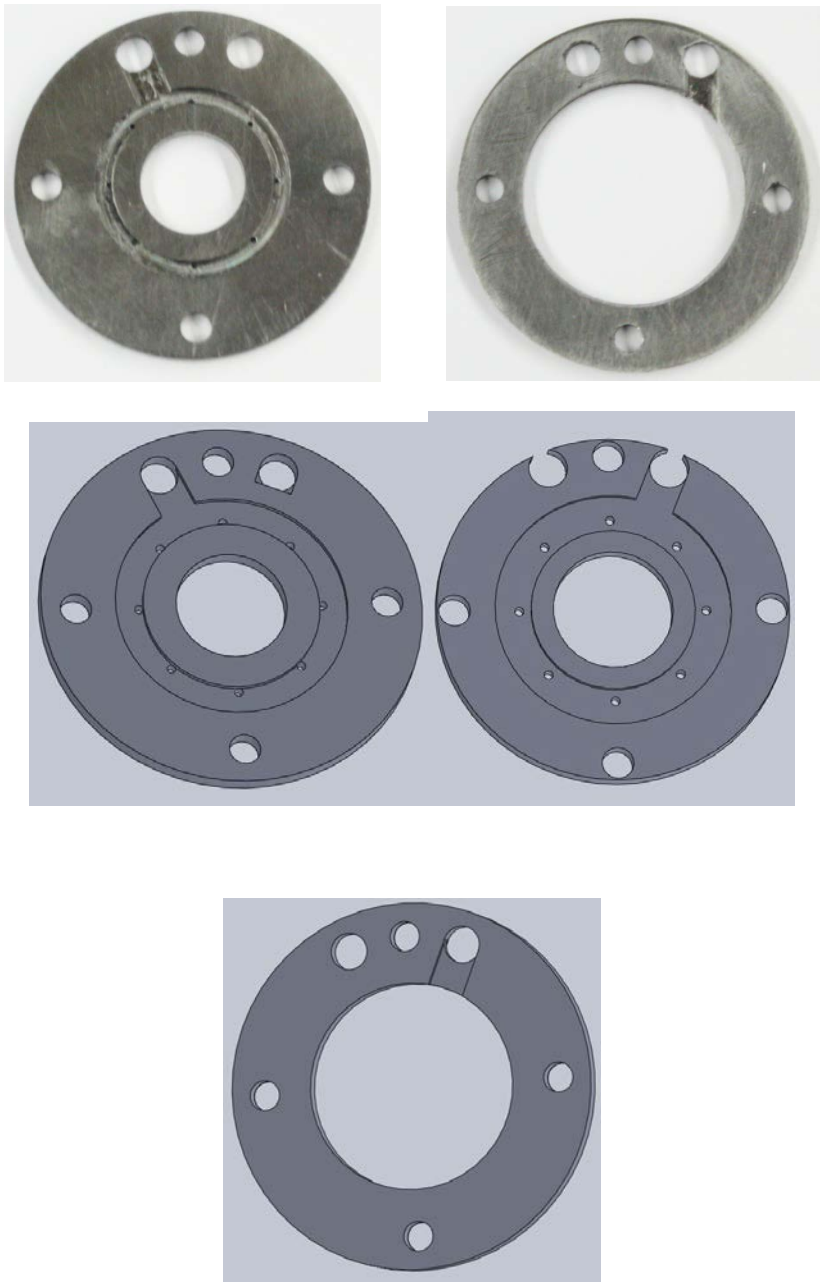

Figure 2.11: Photo of front, rear & spacer air thrust bearing and the thrust spacer.

The air thrust bearings have slots and eight equally spaced hydrostatic air supply orifice holes with 0.25mm dia. The inner and outer diameters of the thrust bearing are 7mm and 12mm,

respectively. A dummy disc with 12mm OD was assembled on to the front end of the rotor to imitate an impeller and to balance the weight distribution along the axial direction.

2.3. Rotordynamic Test 2

Figure 2.12 shows cross section of the assembled micro motor with foil bearings made of Design II elastic foundations, and Figure 2.13 shows the micro motor mounted on a pedestal for test. Two fiber optic probes were used to measure rotor vibration along vertical and horizontal directions. Cooling air for the bearings was injected from the front cover of the motor end flowing through the thrust bearing and get to the ambient through the journal bearing. This cooling system also provide air to the hydrostatic thrust disk injected through the small holes to the thrust runner of the motor.

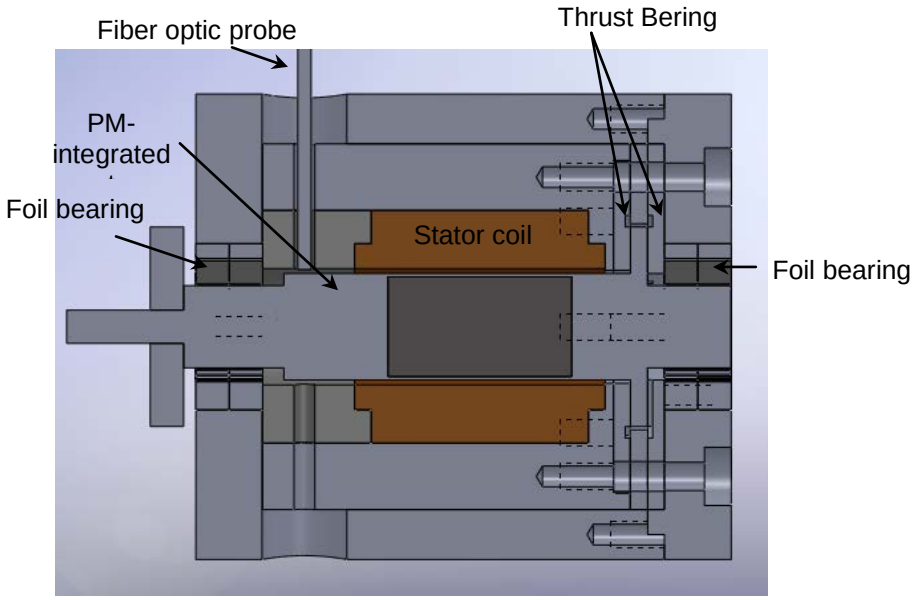

Figure 2.12: Cross section of assembled motor drive with foil bearings; cooling jackets are now shown

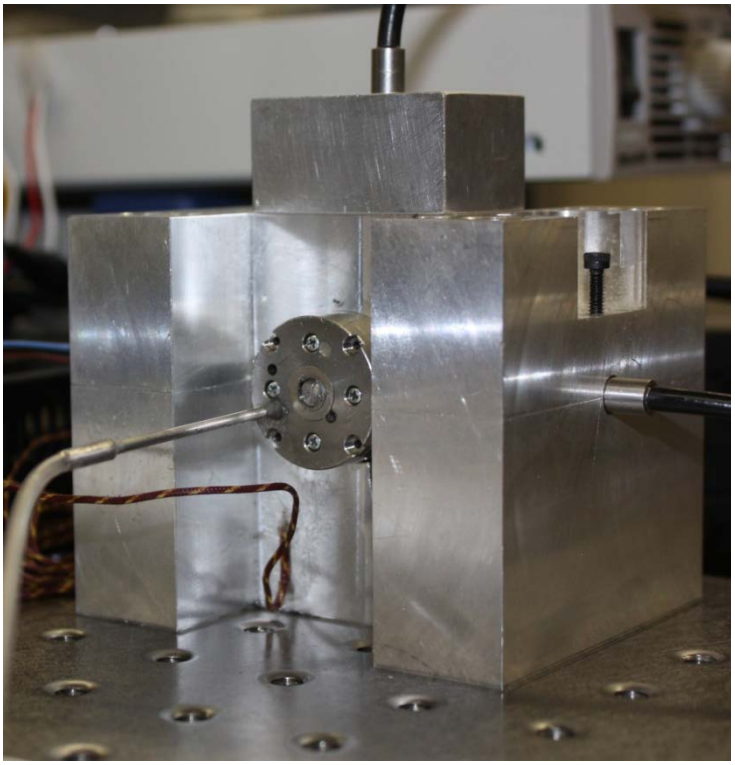

Figure 2.13: Photo of the new rig with two fiber optic probes

The micro motor is powered by a motor controller with a rated speed of 500,000rpm with 24~75 VDC supply provided by Celeroton Technology, Zurich, Switzerland.

Figure 2.20 presents waterfall plots of the rotor vibrations along both horizontal and vertical directions up to 350,000 rpm. Back electromotive force (EMF) from the stator coil reached about 22V when the speed reached at 350,000 rpm with 24V DC power supply was used. No subsynchronous vibration was observed up to the test speed.

The test was performed again and this time 80V power supply was used to overcome the back EMF from the stator coil and 400,000 rpm was achieved successfully. But the hydrodynamic pressure developed inside the journal bearing was so high that the top foils as well as the elastic foundations came off and we stopped the spin.

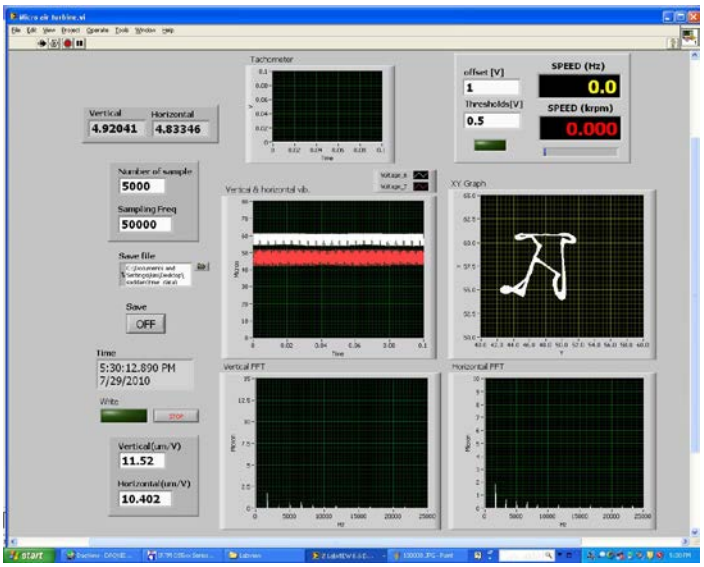

Figure 2.14: Vibration signal at 100K RPM in LabView

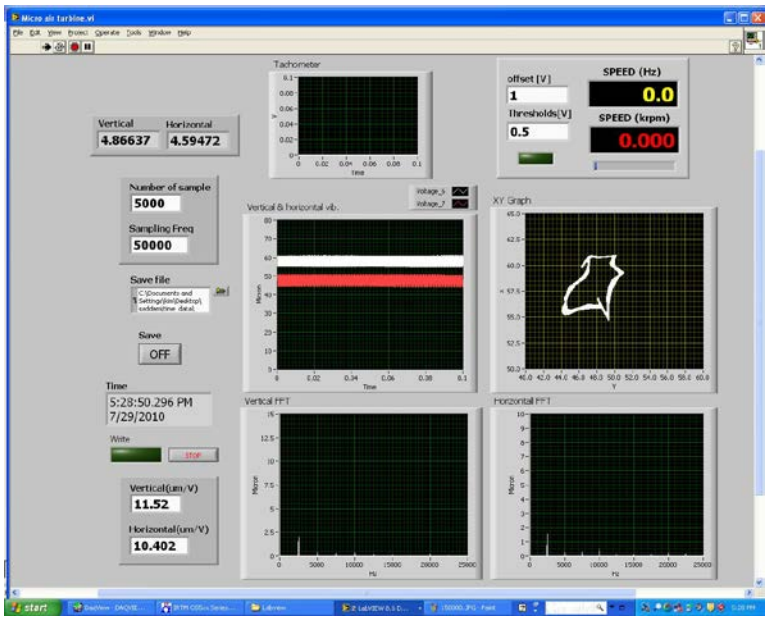

Figure 2.15: Vibration signal at 150K RPM in LabView

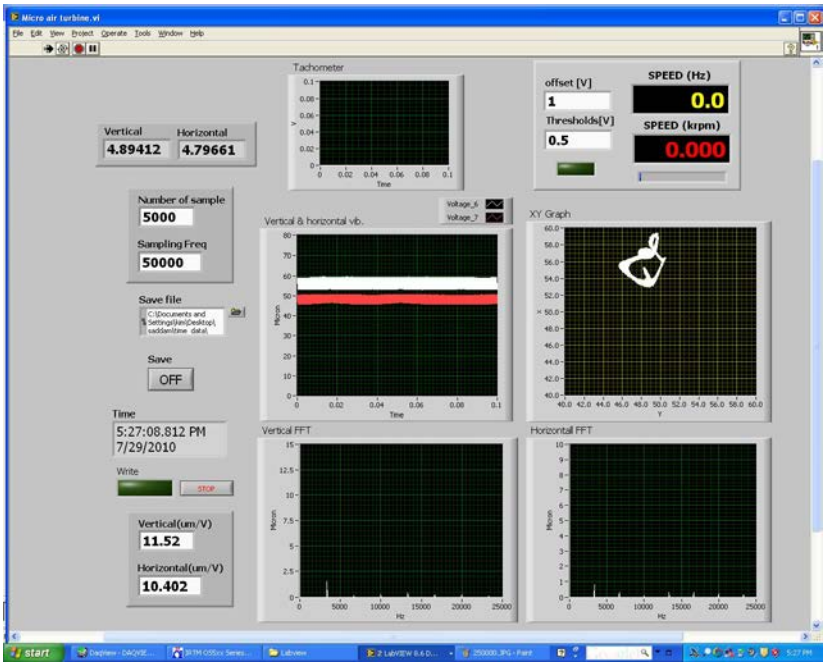

Figure 2.16: Vibration signal at 200K RPM in LabView

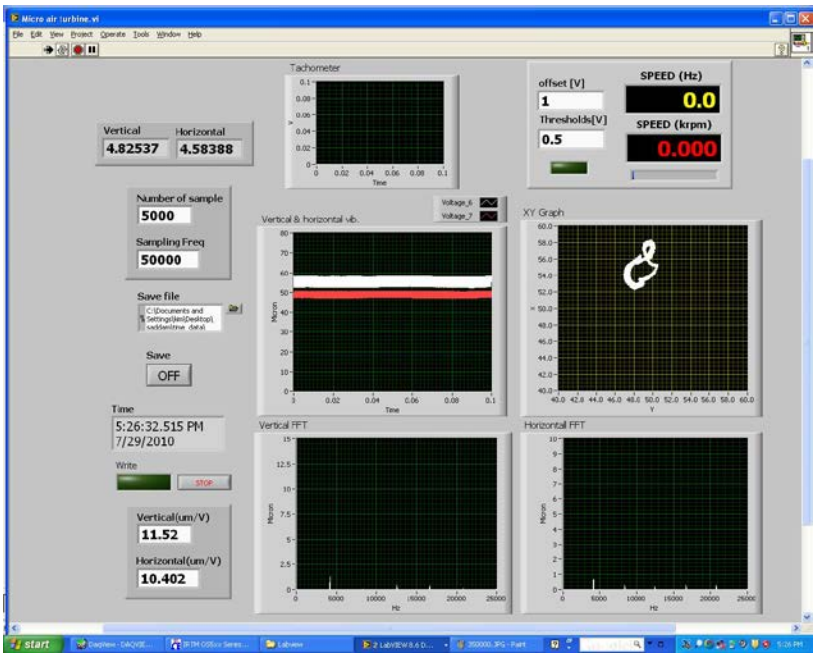

Figure 2.17: Vibration signal at 250K RPM in LabView

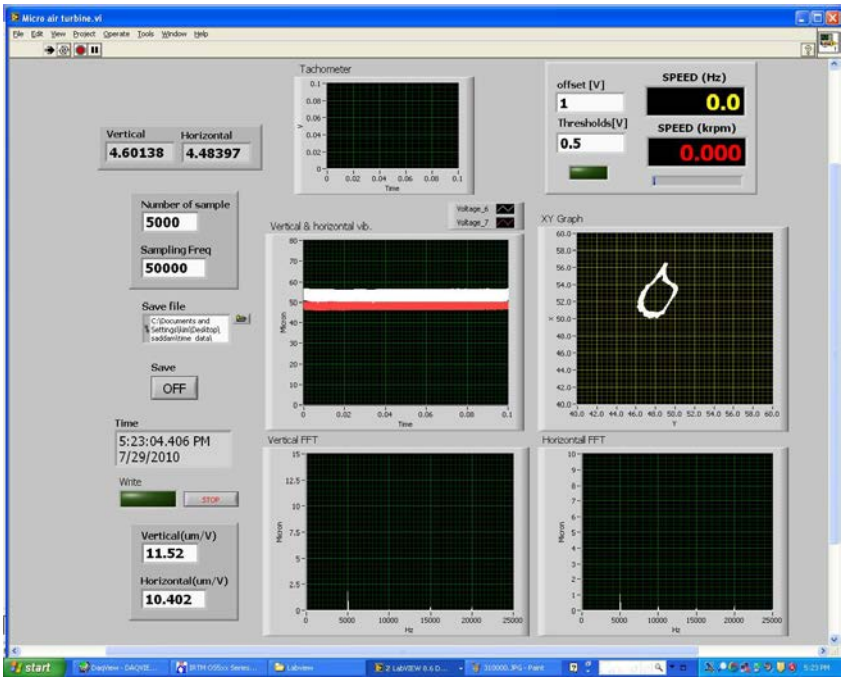

Figure 2.18: Vibration signal at 300K RPM in LabView

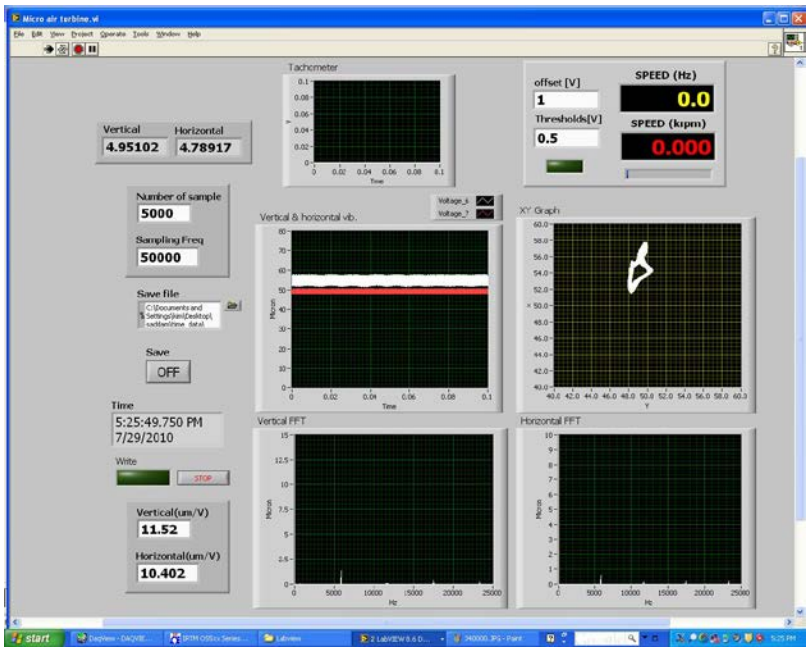

Figure 2.19: Vibration signal at 350K RPM in LabView

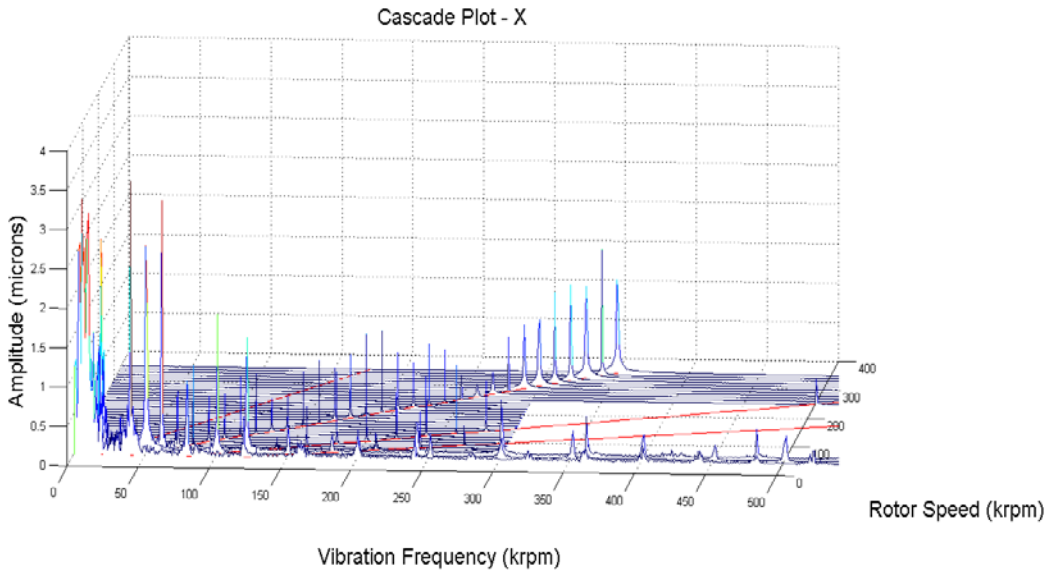

(a)

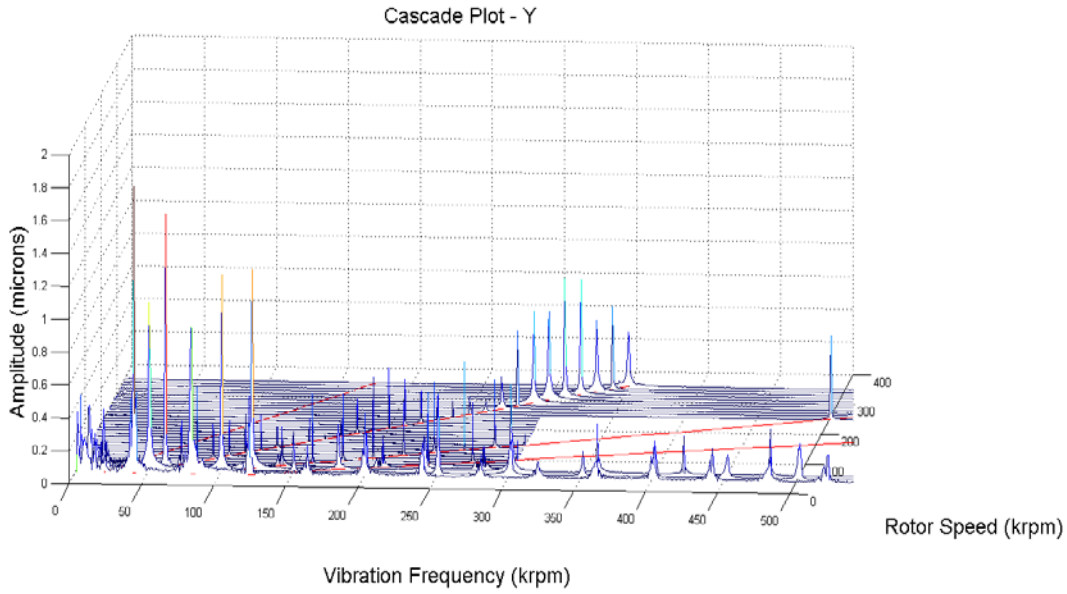

(b)

Figure 2.20: Waterfall plots from measured vibration signals, (a) Horizontal direction, (b) Vertical direction

2.4. Rotodynamic Test 3

A new bump foil bearing with corrugated bump foils made of Inconel® 718 was designed and manufactured as shown in Figure 2.21 In terms of manufacturing concern Inconel foil bearing are less expensive then MEMS foil bearing and at same time precision cold forming and heat treating of the inconel bearing is better. Compare to MEMS foil bearing inconel foil bearing are simple and easy to assemble as placing the elastic foundation of MEMS bearing on its seat is a challenging issue cause in most of the cases additional steps should take to overcome this difficulty like using silicon rubber inside the elastic foundation to fix it on its seat.

Figure 2.21: Optical image of manufactured Design III Corrugate Bump Foil Bearing

We used the same test rig, cross section of the assembled micro motor shows in Figure 2.21 with foil bearings made of Design III corrugated bump foils, and Figure 2.13 shows the same micro motor mounted on a pedestal for test. Two fiber optic probes measured rotor vibration along vertical and horizontal directions. Cooling air for the bearings was provided from the front end.

Figure 2.22 presents waterfall plots of the rotor vibrations along horizontal up to 410,000 rpm and vertical directions up to 350,000 rpm as there were some problems in fiber optic probe at time data collection through LabView data acquisition software. As the back electromotive force

(EMF) from the stator coil reached about 22V when the speed reached at 350,000 rpm we used 80V DC power supply to provide sufficient potential to overcome reverse voltage. Major sub-synchronous vibration was observed after 350,000~360,000rpm as well as the synchronous vibration as the author observed that the foil bearing already being failed after 370,000rpm.

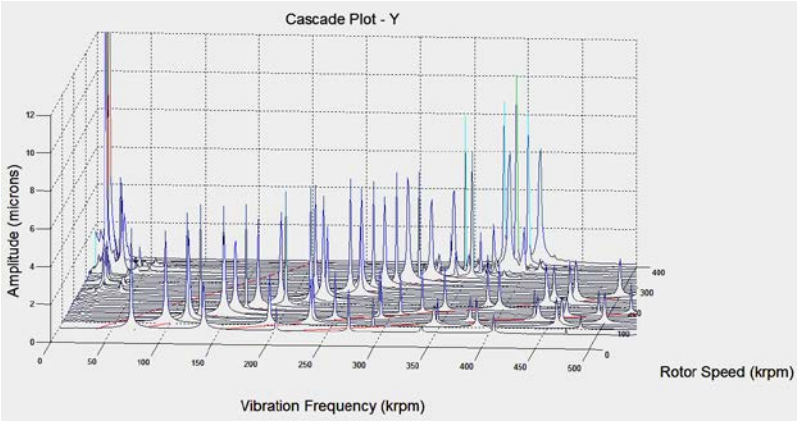

(a)

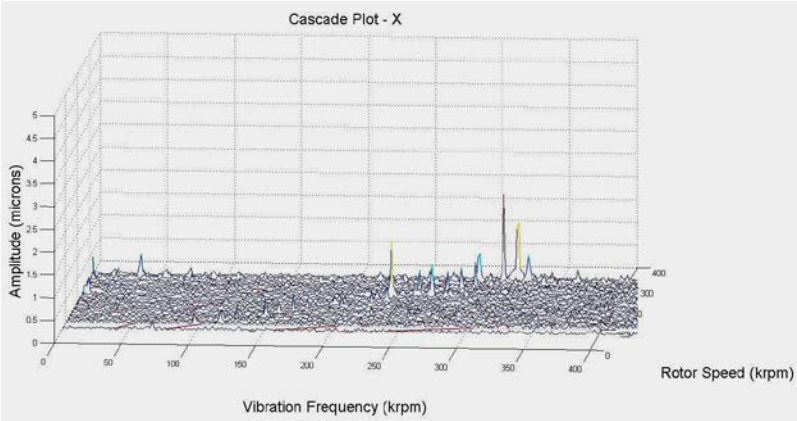

(b)

Figure 2.22: Waterfall plots from measured vibration signals, (a) Horizontal probe, (b) Vertical probe.

Major challenge for the spin test was overcoming the initial friction of the journal bearing from start to low speed, but the bearing performed well when the shaft lift off for the sufficient hydrodynamic pressure developed inside the bearing in high speed (50,000~70,000 rpm).

At time of running rotor was stuck some time inside the journal bearing as it was very difficult to maintain the center line of all the journal bearings exactly at a same line which has a significant effect for rotorbearing performance especially for mesoscale. Another reason was the nonuniform pressure distribution along the both sides of the hydrostatic thrust bearing which caused interaction between the thrust disk and thrust runner which eventually stopped the spinning.

Due to high pressure developed at the time of very high speed (~370,000-400,000 rpm) the top foil of the bearing came off from the bearing sleeve which prevents to continue running the test.

Dummy impeller also falls off twice both for the design II and design III foil bearing even if the screw to fasten the impeller was tightened enough.

The author suspect there are some vibration mode on the rotor that prevents higher speeds and bearing failure at 370,000~400,000 rpm.

A complete new design of the rotor bearing system as well as the electric motor drive, compressor impeller with volute and diffuser and was represent in Chapter 4.

CHAPTER 3

DESIGN & SIMULATION OF MICRO COMPRESSOR

2nd objective is to design a centrifugal compressor which we can use for final test of the motor bearing performance and also the performance of the compressor itself. We use an Excel Spread sheet utilizing the velocity equation to find different flow parameters like mass flow, temperature and geometric parameters like the blade angle in both inlet and outlet. The formulas to calculate the blade angle at inlet and outlet using certain mass flow and pressure ration and also geometry in both inlet and outlet are as follows.

3.1. Theory and Governing Equations for calculating design points

In order to find the optimum design point for the given geometry i.e. impeller exit diameter, impeller height, mass flow, etc velocity equations [21] for both inlet and exit condition is used to determine the inlet and exit blade angle for the impeller maintaining Mach number below one. We use the following equations and relation to calculate optimum design point using a excel spread sheet.

Circumferential velocity at inlet:

$$U_1 = \frac{D_1}{2} \times \omega \tag{1}$$

Inlet stage Area:

$$A_1 = \pi \times D_1 \times h_1 \tag{2}$$

Circumferential velocity at outlet:

$$U_2 = \frac{D_2}{2} \times \omega \tag{3}$$

Outlet stage Area:

$$A_2 = \pi \times D_2 \times h_2 \quad (4)$$

Equation 1 and 3 are for calculating velocity at the tip of the blade and Equation 2 and 4 are for the areas at inlet and exit.

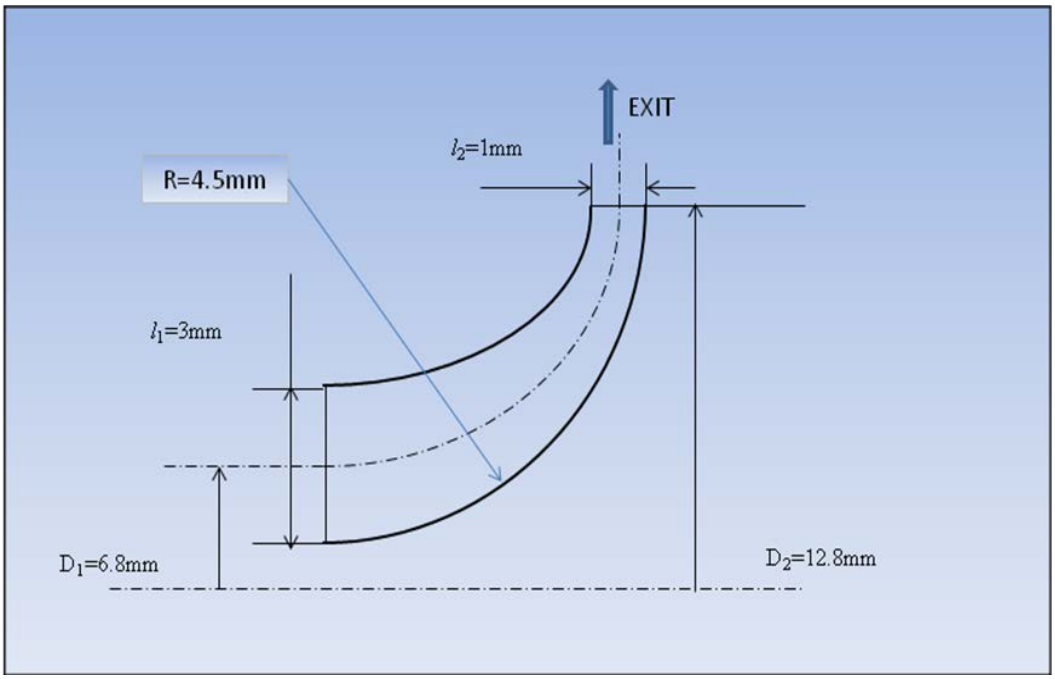

Figure 3.1: Meridional Plane of the centrifugal compressor

Here,

D_1 = Mean Diameter at inlet

D_2 = Mean Diameter at outlet

ω = rotational speed

l_1 = blade height at inlet

l_2 = blade height at outlet

α_1 = Inlet flow angle

α_2 = Exit flow angle

Given data:

Stage pressure ratio: $\frac{P_2}{P_1}$

$\dot{m}$ =Compressor stage mass flow

$T_0 = T_1 =$ Compressor inlet temperature

η =stage efficiency

For every calculation we change the pressure ratio, and mass.

Air properties:

R = Gas constant

c_p = Specific heat

k = Specific heat ratio

P_a = Ambient pressure

Volume flow, $Q = A \times V$

Mass flow, $\dot{m} = Q \times \rho$

Density, $\rho = \frac{P}{R \times T}$

All these parameters shown above except mass flow are fed as a fixed value in the Excel spread sheet.

Radial Velocity,

$$C_r = V = \frac{Q}{A} = \frac{\dot{m}}{\rho \times A} = \frac{\dot{m} \times R \times T}{P \times A} \tag{5}$$

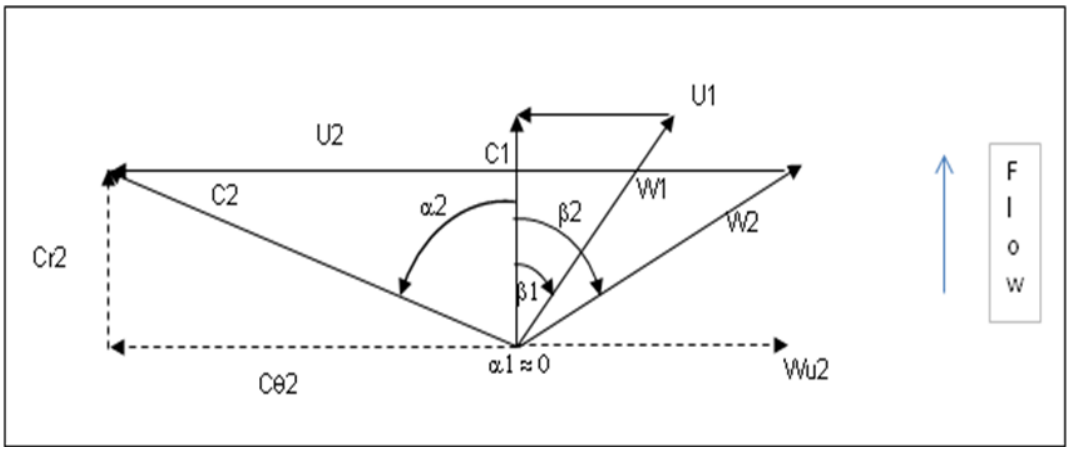

Figure 3.2: Velocity diagram

Thermodynamic energy equations and velocity triangle were used in both inlet and outlet of the compressor to calculate the blade angle at both inlet and outlet maintaining mach number below one.

Properties at the mean diameter:

At inlet:

$$T_1 = T_0$$

$$P_1 = P_a$$

Enthalpy of gas at inlet $$h_1 = c_p \times T_1 \tag{6}$$

Kinetic Energy at inlet $$K_1 = \frac{C_1^2}{2} \tag{7}$$

Total energy at inlet $$H_1 = h_1 + K_1 \tag{8}$$

Radial component of C_1 $$C_{r1} = \frac{\dot{m} \times R \times T_1}{P_1 \times A_1} \quad (9)$$

Tangential component of C_1 $$C_{\theta 1} = C_{r1} \tan(\alpha_1) = 0 \quad (10)$$

Tangential component of W_1 $$W_{\theta 1} = U_1 - C_{\theta 1} = U_1 \quad (11)$$

Inlet absolute flow velocity $$C_1 = \sqrt{C_{\theta 1}^2 + C_{r1}^2} = C_{r1} \quad (12)$$

Radial component of W_1 $$W_{r1} = C_{r1} = C_1 \quad (13)$$

Inlet Relative flow velocity $$W_1 = \sqrt{W_{r1}^2 + W_{\theta 1}^2} = \sqrt{C_1^2 + U_1^2} \quad (14)$$

Inlet relative flow angle (blade angle) $$\beta_1 = \tan^{-1}\left(\frac{W_{\theta 1}}{C_{r1}}\right) \quad (15)$$

Mach number at inlet $$M_{a1} = \frac{W_1}{\sqrt{k \times R \times T_1}} \quad (16)$$

At outlet isentropic:

$$P_{2s} = P_2$$

$$T_{2s} = T_0\left(\frac{P_2}{P_1}\right)^{\frac{k-1}{k}} \quad (17)$$

$$h_{2s} = c_p \times T_{2s} \quad (18)$$

$$K_{2s} = \frac{C_{2s}^2}{2} \quad (19)$$

$$H_{2s} = h_{2s} + K_{2s} \quad (20)$$

$$C_{r2s} = \frac{\dot{m} \times R \times T_{2s}}{P_{2s} \times A_{2s}} \quad (21)$$

$$C_{\theta 2s} = C_{r2s} \tan \alpha_{2s} \quad (22)$$

At outlet:

$$T_2 = T_1 + \frac{T_{2s} - T_1}{\eta} \quad (23)$$

Enthalpy of gas at outlet $$h_2 = c_p \times T_2 \quad (24)$$

Kinetic Energy at outlet $$K_2 = \frac{C_2^2}{2} \quad (25)$$

Total energy at outlet $$H_2 = h_2 + K_2 \quad (26)$$

Radial component of C_2 $$C_{r2} = \frac{\dot{m} \times R \times T_2}{P_2 \times A_2} = \frac{\dot{m} \times R \times T_1}{P_1 \times \pi \times D_2 \times h_2 \times \eta} \left\{ \frac{(\eta - 1) + \left(\frac{P_2}{P_1}\right)^{\frac{k-1}{k}}}{\left(\frac{P_2}{P_1}\right)} \right\} \quad (27)$$

Tangential component of C_2 $$C_{\theta 2} = C_{r2} \tan \alpha_2 \quad (28)$$

Tangential component of W_2 $$W_{\theta 2} = U_2 - C_{\theta 2} \quad (29)$$

Radial component of W_2 $$W_{r2} = C_{r2} \quad (30)$$

Exit absolute flow velocity $$C_2 = \sqrt{C_{\theta 2}^2 + C_{r2}^2} \quad (31)$$

Exit relative flow velocity $$W_2 = \sqrt{W_{r2}^2 + W_{\theta 2}^2} \quad (32)$$

Exit relative flow angle (blade angle) $$\beta_2 = \tan^{-1}\left(\frac{W_{\theta 2}}{C_{r2}}\right) \quad (33)$$

Mach number at outlet $$M_{a2} = \frac{W_2}{\sqrt{k \times R \times T_2}} \quad (34)$$

From equations (6)-(8), (18)-(20) and (24)-(26) are corresponding energy equation calculated in inlet and outlet and also isentropic values at the outlet. Velocity triangles (Figure 3.2 & Figure 3.3) were used to calculate the velocity terms (Equations (9)-(14) and (27)-(32))

corresponding inlet and outlet to find the metal angle $\beta_1 \& \beta_2$ (Equations(15) and (33)). Flow relative Mach numbers are also calculated by using the Equations (16) and(34).

Stage mechanical energy (specific mechanical energy) and stage power are defined using the following two equations

$$l_{\mathrm{m}} = U_1 \times C_{\theta 1} + U_2 \times C_{\theta 2} \tag{35}$$

Stage power

$$\mathrm{P} = \dot{m}\left(H_2 - H_1\right) \tag{36}$$

Selection of Design Point:

All calculation in (Table 3.1, Table 3.2 & Table 3.3) are done by using all equations from Equation (1) to Equation (36) in the excel spread sheet. The highlighted point is selected for designing the compressor. Rated speed of 700,000 rpm and Mach number for both inlet and outlet maintains below one. As we can see at rated speed this type of compressor can provide enough air supply up to three 1kW Solid Oxide Fuel Cells (SOFC)[22] as the 1kW fuel cell needs 3g/s of air supply.

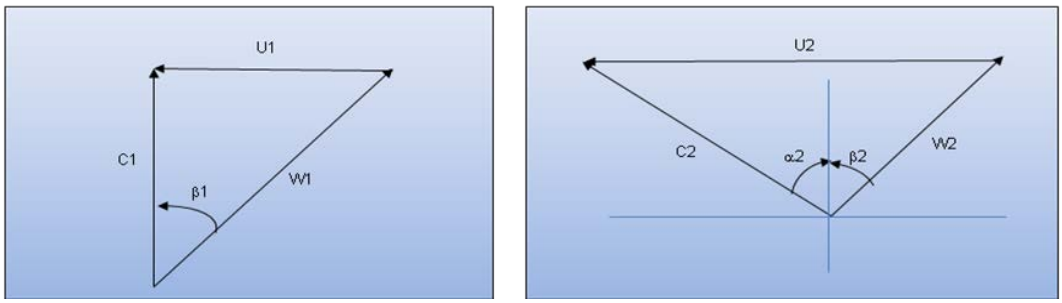

(a) (b)

Figure 3.3: Velocity Triangle at (a) Inlet and (b) Outlet

Table 3.1: Parameters at inlet of the impeller

At Inlet

Sonic Velocity $= \sqrt{k \times R \times T_1} = 343 m/s$

$\dot{m}$	C_1	N	U_1	W_1	M_{a1}	β_1
1gm/s	13 m/s	1.00 million	356 m/s	357 m/s	1.05	88°
5 gm/s	65 m/s	0.95 million	338 m/s	343 m/s	1.00	80°
10 gm/s	130 m/s	0.90 million	323 m/s	343 m/s	1.00	68°
10 gm/s	130 m/s	0.85 million	300 m/s	329 m/s	0.96	66°
11 gm/s	143 m/s	0.85 million	303 m/s	335 m/s	0.97	65°
12 gm/s	156 m/s	0.80 million	285 m/s	324 m/s	0.95	62°
10 gm/s	**210 m/s**	**0.70 million**	**250 m/s**	**280 m/s**	**0.82**	**26°**

Table 3.2: Parameters at the exit of the impeller

At Outlet

Sonic Velocity $= \sqrt{k \times R \times T_2} = 409 m/s$; Stage pressure ratio : $\frac{P_2}{P_1} = 3.0$

$\dot{m}$	C_2	N	U_2	W_2	M_{a2}	β_2
15 g/s	293 m/s	1.00 million	670 m/s	441 m/s	1.08	90-70°
10 g/s	195 m/s	1.00 million	670 m/s	510 m/s	1.25	90-79°
10 g/s	195 m/s	0.95 million	637 m/s	478 m/s	1.17	90-78°
10 g/s	195 m/s	0.90 million	604 m/s	444 m/s	1.09	90-77°
10 g/s	195 m/s	0.85 million	570 m/s	412 m/s	1.01	90-76°
10 g/s	195 m/s	0.80 million	536 m/s	380 m/s	0.93	90-75°
10 g/s	**130 m/s**	**0.70 million**	**440 m/s**	**280 m/s**	**0.68**	**22°**
8 g/s	156 m/s	0.75 million	502 m/s	378 m/s	0.92	90-78°
11 g/s	214 m/s	0.85 million	570 m/s	398 m/s	0.97	90-75°

Table 3.3: Comparison between inlet and exit to find optimum design Point

Inlet &Outlet comparison

Stage pressure ratio : $\frac{P_2}{P_1} = 3.0$

$\dot{m}$	N	M_{a1}	M_{a2}	β_1	β_2
15 g/s	1.00 million	1.18	1.08	90-61°	90-70°
10 g/s	**0.70 million**	**0.82**	**0.68**	**28°**	**22°**
10 g/s	0.90 million	1.01	1.09	90-68°	90-77°
10 g/s	0.85 million	0.96	1.01	90-66°	90-76°

Selection of different geometric parameter such as Diameter at inlet and exit, Blade height at inlet and exit, curvature of the blade profile etc are defined as following

Table 3.4: Different geometric parameters for Solid modeling

Geometric Parameters	Values
Diameter at Inlet	1.9mm
Blade Height at Inlet	3mm
Diameter at Exit	12mm
Blade Height at Exit	1mm
Impeller Height	5.5mm
Inlet Blade Angle	28°
Exit Blade Angle	22°

3.2. Mathematical modeling and Numerical Simulation process

In order to accurately simulate the internal fluid flow within a centrifugal compressor, the Favre-averaged Navier-Stokes equations were solved using commercial software. Furthermore, commercially available mesh generation and computer aided design (CAD) programs were used

to define the geometry and grid generation. This section will briefly review some of the mathematical modeling and numerical solution procedures.

3.2.1.Fluid flow equations

Navier-Stokes Equations:

The fundamental equations that describe fluid flow behavior are the Navier-Stokes equations. This is a set of five (two scalar and 1 vector) partial differential equations that describe the conservation of mass, momentum and energy. The integral form of the Navier-Stokes equations is as follows

$$\frac{\partial}{\partial t}\int_v \rho dv + \int_S \rho U_j dn_j = 0 \tag{37}$$

$$\frac{\partial}{\partial t}\int_v \rho U_i dv + \int_S \rho U_j U_i dn_j = -\int_S P dn_j + \int_S \mu_{eff}\left(\frac{\partial U_i}{\partial x_j} + \frac{\partial U_j}{\partial x_i}\right) dn_j + \int_v S U_i dv \tag{38}$$

$$\frac{\partial}{\partial t}\int_v \rho\phi dv + \int_S \rho U_j \phi dn_j = \int_S \Gamma_{eff}\left(\frac{\partial \phi}{\partial x_j}\right) dn_j + \int_v S\phi dv \tag{39}$$

where ρ is the density, v is the volume, U_i is the velocity component, d_{nj} are elemental surface area, μ_{eff} is the effective coefficient of viscosity, S_{ui} is a momentum source term, φ is the internal energy per unit mass, Γ_{eff} is the effective net heat flux and S_φ is the energy source term.

Turbulence modeling:

Turbulent flows occur at high Reynolds number as the velocity of the impeller were very high ~ 500,000-700,000 rpm), when the inertia of the fluid overwhelms the viscosity of the fluid, causing the laminar flow motions to become unstable. Under these conditions, the flow is

characterized by rapid fluctuations in pressure and velocity which are inherently three dimensional and unsteady. Turbulent flow is composed of large eddies that migrate across the flow generating smaller eddies as they go. These smaller eddies in turn generates smaller eddies until they become small enough that their energy is dissipated due to the presence of molecular viscosity. The full influence of the turbulent fluctuations on the mean flow must be modeled. We used Standard Launder and Sharma $k-\varepsilon$ turbulence model in CFD solver.

CAD geometries for this study were generated in Bladegen and SolidWorks. SolidWorks and BladeGen at its core is a full functioned CAD solid modeling tool that is widely used in the aerospace industry. This CAD tool was used for this thesis to define the geometries for the compressor stage as shown in Figure 2. Two different shrouded compressor was modeled by using Bladegen and SolidWorks as first one had 12 blades(6 main and 6 spliter) and the other one had 10 blades (5 main and 5 spliter). A Structured mesh for fluid flow region was done in ICEM CFD by blocking technique (See Appendix).

Bladegen:

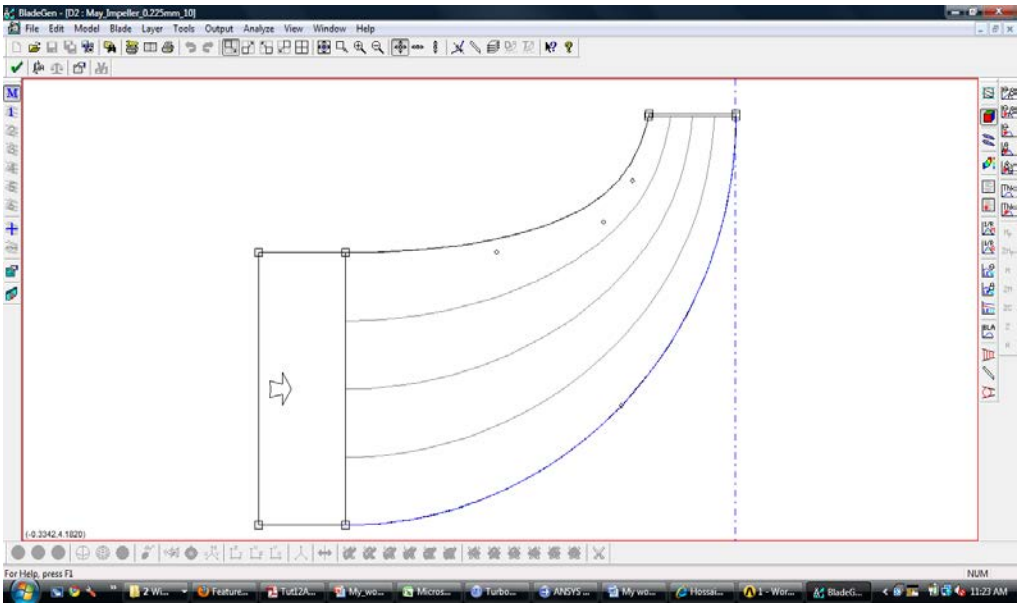

Figure 3.4: Inputting Meridional Geometry information of the blade profile in the BladeGen

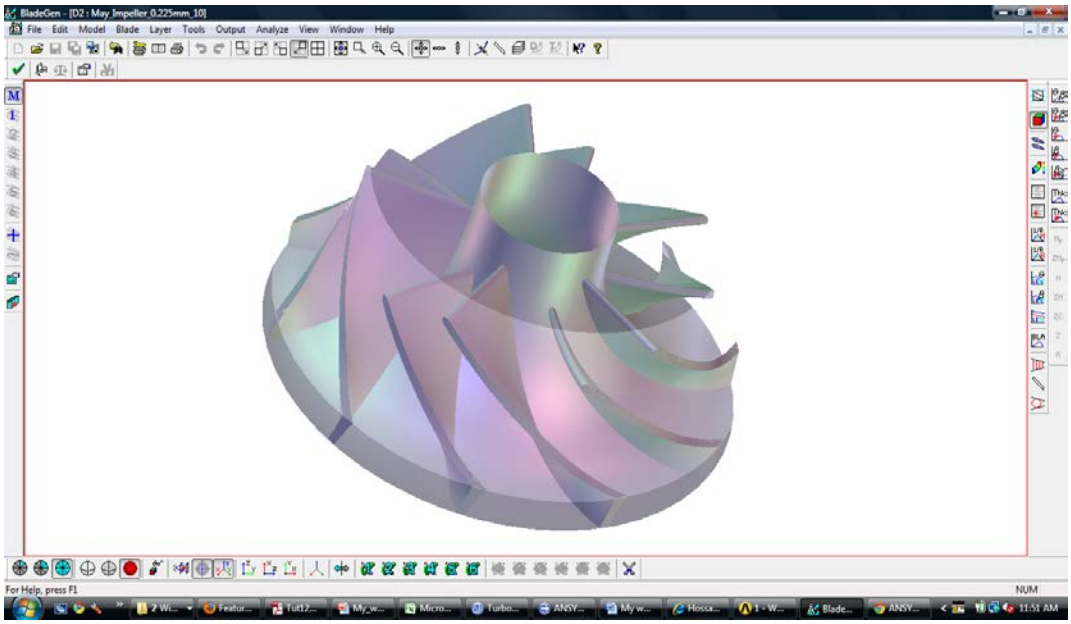

Figure 3.5: Solid Model in BladeGen

3.2.2.CAD geometry Definition for the Flow Region

For flow geometry definition Ansys TurboGrid is used as a key benefit of TurboGrid is that it can create the file format which is integrates smoothly with ANSYS ICEM CFD allowing the complex geometries generated in BladeGen to be easily and reliably imported into ANSYS ICEM-CFD.

TurboGrid:

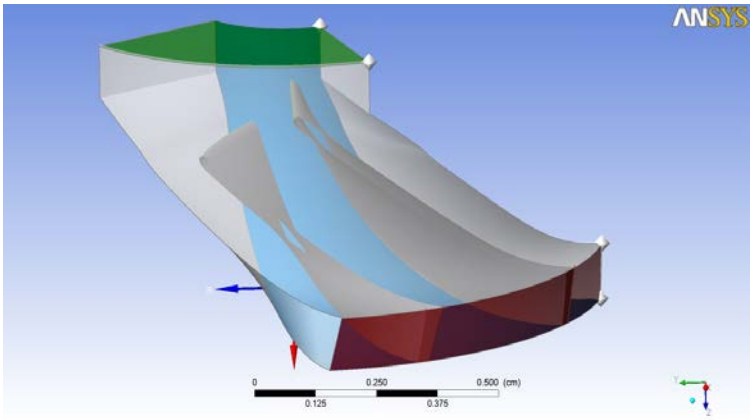

Figure 3.6: Geometry of the Fluid Flow Region exported from Bladegen

In Figure 3.6: Geometry of the Fluid Flow Region exported from Bladegen Shows a 3D Fluid flow region of single periodic geometry. Solid model of the blade profile was exported to TurboGrid for creating fluid flow region over the blade to generate mesh. There are two different geometries for two different blade numbers (12 and 10). As we simulate a shrouded impeller so tip clearance at shroud should be zero.

3.2.3.Mesh Generation

ICEM CFD:

Meshing is the most critical part of the simulation process. The mesh as well as the process has a great effect on simulation results whether the results are accurate enough compare to the expected design point and also the convergence to the result also depending on it. Mesh generation was performed using ANSYS ICEM-CFD (APPENDIX C). This program was chosen because it is full featured and it is compatible with a wide range of CAD and commercial computational fluid dynamics software.

With ANSYS ICEM-CFD, it is possible to import CAD geometry and generate both structured and unstructured meshes based on it. For this thesis, the impeller section consisted of structured hexahedral meshes as shown in Figure 3.8 to Figure 3.9 while as structured mesh is very important regarding accuracy and convergence. We use “Blocking” technique to create structured mesh.

The ANSYS ICEM-CFD hexahedral mesh generator is an object-based, semi-automatic, multi-block structured or unstructured, surface and volume mesh generator. The block topology model is generated directly on, but independent of, the underlying CAD geometry. It is recognized as one of the fastest commercially available hexahedral mesh generation tools. ANSYS ICEM-CFD is projection based in that the surfaces of the mesh are automatically projected on to the nearest CAD surface. It is also possible to specify the projection of points, edges and surfaces for a greater degree of control.

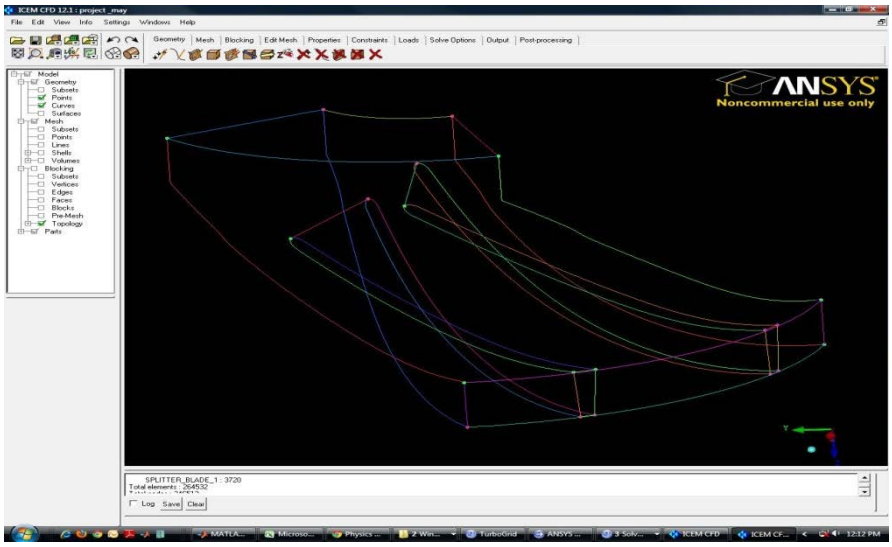

Figure 3.7: Geometry exported from TurboGrid

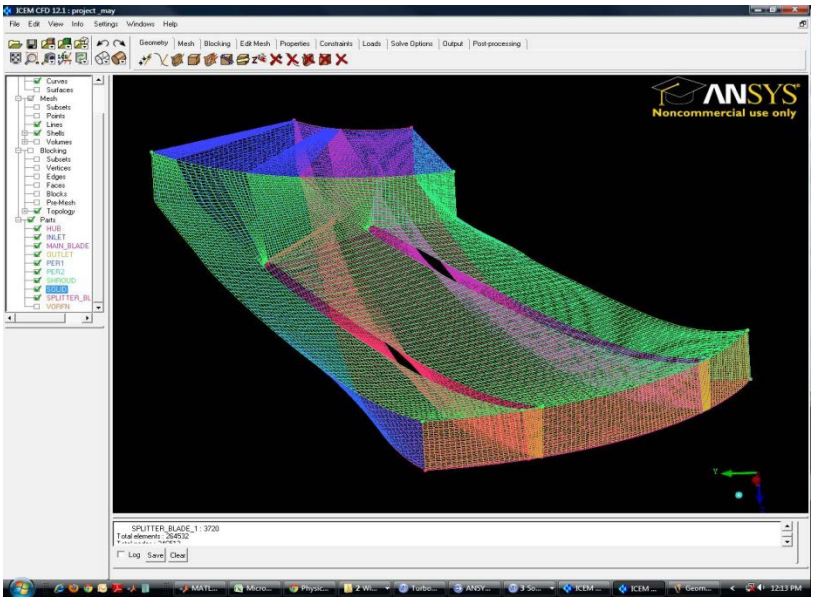

Figure 3.8: Surface Mesh

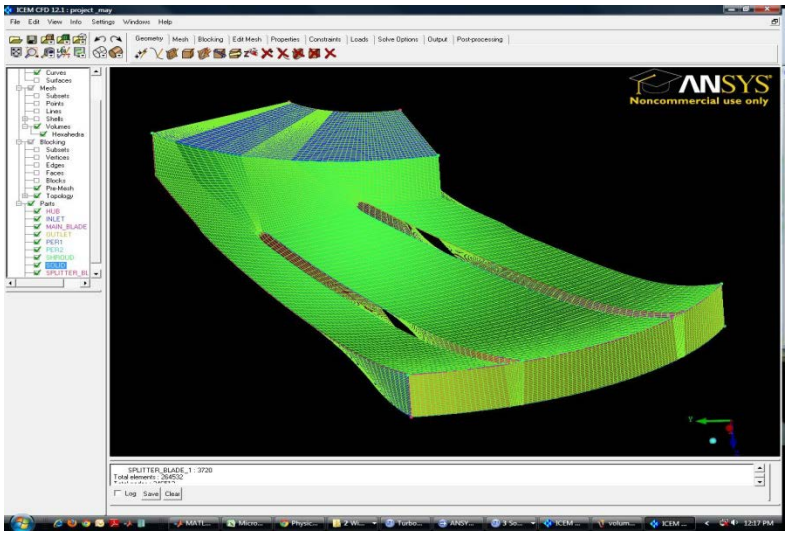

Figure 3.9: Volume Mesh

3.2.4.CFX Flow Solver

The computational fluid dynamics solver used in this thesis was ANSYS CFX. CFX is a technology leader, providing highly accurate results especially turbo machinery application, robust solutions and industry-leading parallel efficiency. CFX was chosen because it represented a state of the art commercial CFD solver package able to tackle the complex problems faced in this thesis. A summary of various aspects and properties of the ANSYS CFX flow solver can be found in its online documentation and also in the user manual.

CFX (Pre-processing):

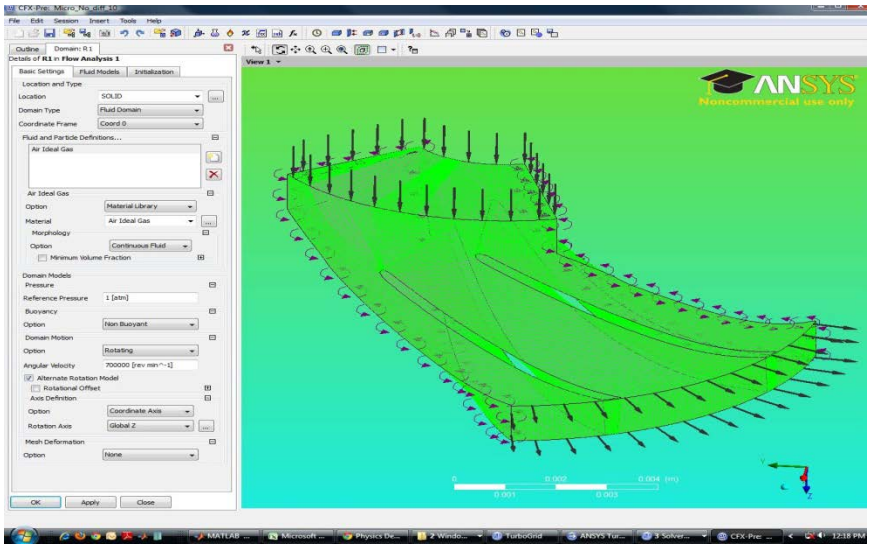

Figure 3.10: Case file created in CFX-Pre

After creating the Mesh we import it to the Solver (Ansys CFX) to simulate the flow field of fluid (air). Several steps involves to this process.

- Check the grid whether there are some negative volume existed or not
- Scale the grid to necessary units (in our case mm).
- Define models (as using Energy eqn, Viscous relations(K-epsilon) etc)
- Define the materials, (fluid-air, solid-aluminum)
- Define the Cell Zone Conditions (inlet, outlet, main passage as fluid-air)
- Define the boundary Conditions in different regions.(the most important and critical part).
- Set the solution methods, solution controls, solution initializations

Due to their complex geometry, centrifugal compressors can be difficult systems to analyze using CFD. CFX offers three ways of handling the passing of the solution content across the domain interfaces between the rotor and the diffuser.

First is the frozen rotor approach where the frame of reference is changed according to the motions defined for the domain, but the relative orientation of the geometry is fixed.

The second method is called the stage averaging. Here circumferential averaging is applied at the interface between the rotating and the stationary domains. This method helps in the convergence of a steady state simulation because the interface solution state is circumferentially uniform. A one-time mixing loss is added by the stage averaging at the interface. This model accounts for the time averaged interaction effect but neglects the transient interaction effect.

The last method is the transient rotor-stator simulation. This is used for fully unsteady simulations to take into account the true transient interactions of the flow between the domains. The main disadvantage of this method is the high cost of the simulations in terms of CPU time and disk space requirements. In this thesis first i.e. frozen rotor approach is used.

CFX (Solver):

The on-design operating conditions was computed first and mesh density and turbulence model studies were conducted to assess mesh requirements for the stage. After the on-design results were deemed satisfactory, three off-design cases were studied.

The initial conditions within the compressor are estimated automatically by CFX based on the boundary conditions. However when the compressor was simulated at operating conditions, the numerical solution was found to diverge. Therefore, a rotational velocity ramping function was used at start up

The impeller rotational velocity at start up was set such that the initial velocity is about 25-30% of the desired velocity and it was increased to the desired velocity over the next 75-100 iterations. This allows the flow to develop at slower rotational velocities such that when the desired rotational velocity is reached, the flow properties within the compressor are much closer to the desired steady-state solution. This technique generates improved estimates for the initial data, which was necessary because of the aggressive time steps (1/rotational velocity) used in

order to quickly reach convergence. As a comparison, this time step is over 10 times larger than the one automatically estimated by CFX based on mesh dimensions.

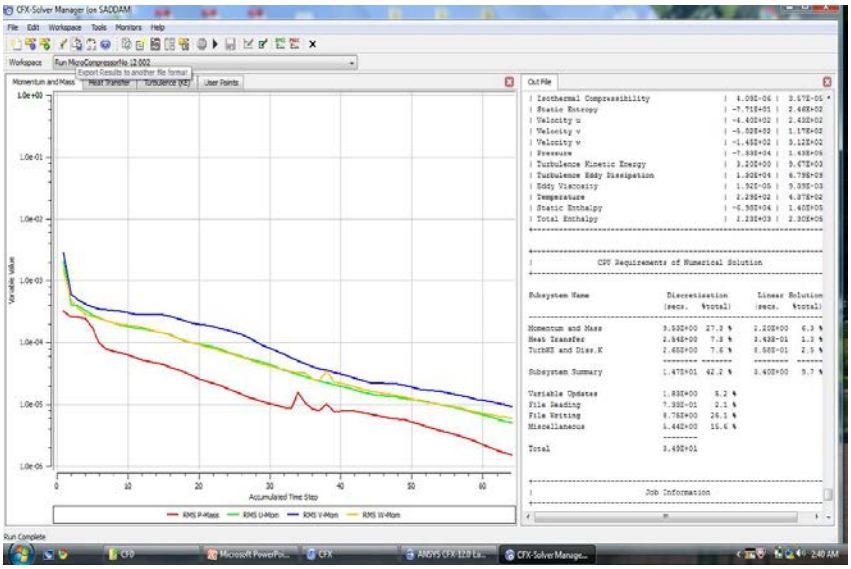

Figure 3.11: Residual of the computations after several iterations in CFX-Solver

We run the case files created from CFX-Pre in the solver to get the simulation results.

- Run the calculations for certain number of iterations
- Use time step as 1/rotational velocity.
- Set maximum error level
- Check the results whether it is Converging or Diverging
- If diverging then we have to change different condition and run the calculations again until we got the Convergence.

3.2.5.Analysis

CFX (Post-processing)

Here we present the Results for the case of Speed= 500,000 rpm, PR=1.9, No of Blades=10 and comparing with a case result from [3, 13] which also run at 500,000 rpm.

Table 3.5: Compressor Performance Results (simulation)

Turbomachinery data	
Rotation Speed	500,000 rpm
Pressure Ratio	1.6
Mass Flow Rate	1.7 g/s
Efficiency	69 %
Mean Diameter at Inlet	6.4 mm
Mean Diameter at Inlet	12 mm
Number of Blades	10
Tip clearance	Zero (shrouded)

Table 3.6: Experimental [3, 13]

Turbomachinery data	
Rated speed	500 000 rpm
Pressure ratio	1.6
Mass flow	2 g/s
Compressor efficiency	72 %
Mean diameter at inlet	5.28 mm
Mean diameter at outlet	10.5 mm
Number of Blades	12
Tip clearance	100 μm

As shrouded impeller were used, for same mass flow higher pressure ratio is observed in low speed and also the speed lines in both simulation and experimental results [3] have similar trend except the chock limit in simulation are appeared later in low pressure at higher mass flow.

Meridional plot for Table 3.5

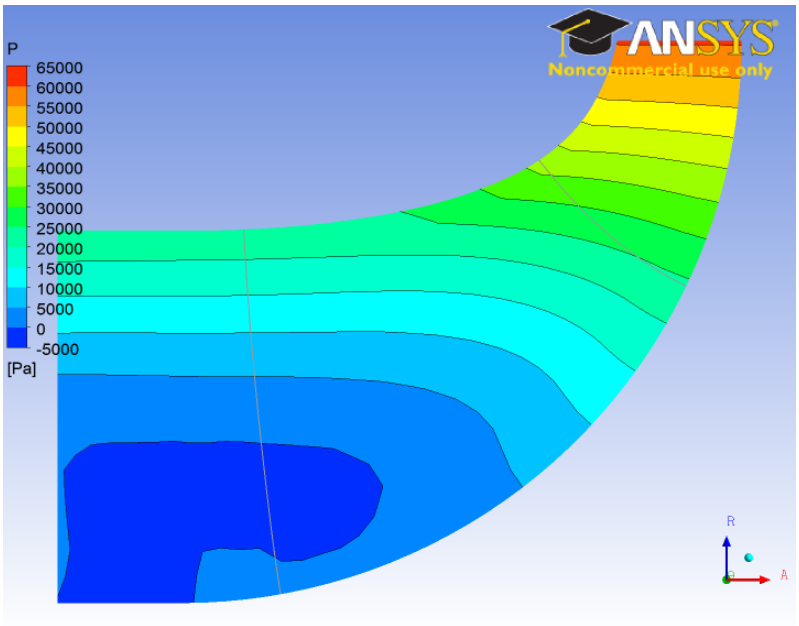

Figure 3.12: Pressure distribution along Meridional plane

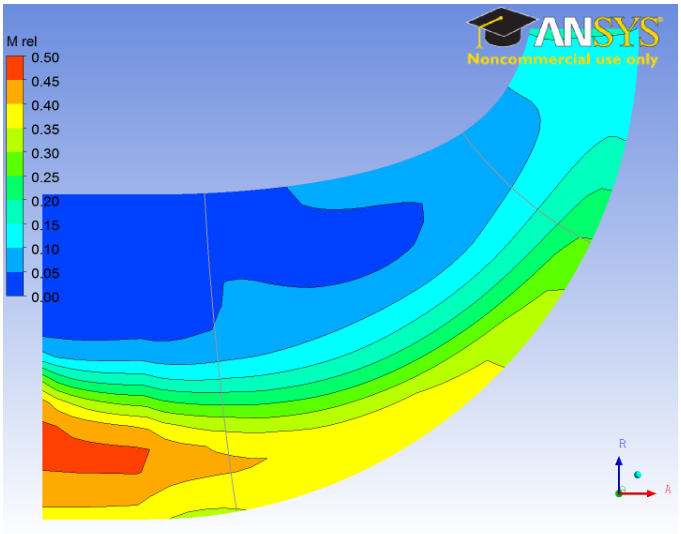

Figure 3.13: Mach number distribution along Meridional plane

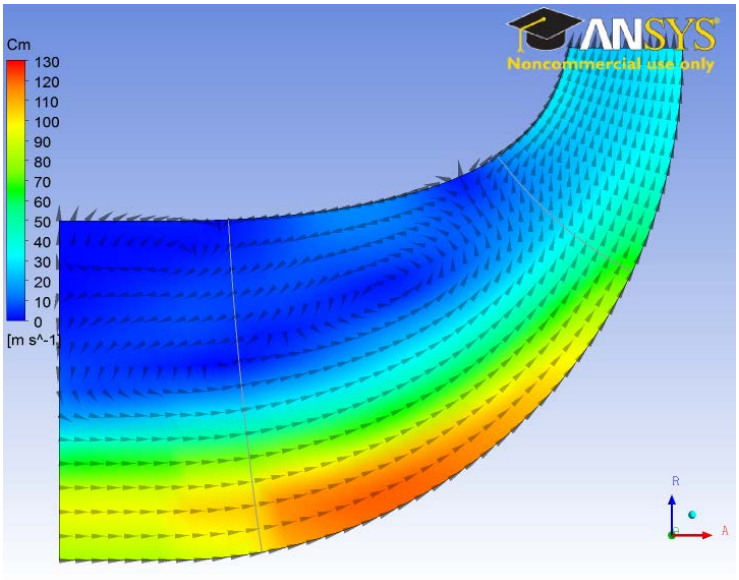

Figure 3.14: Cm on Meridional Surface

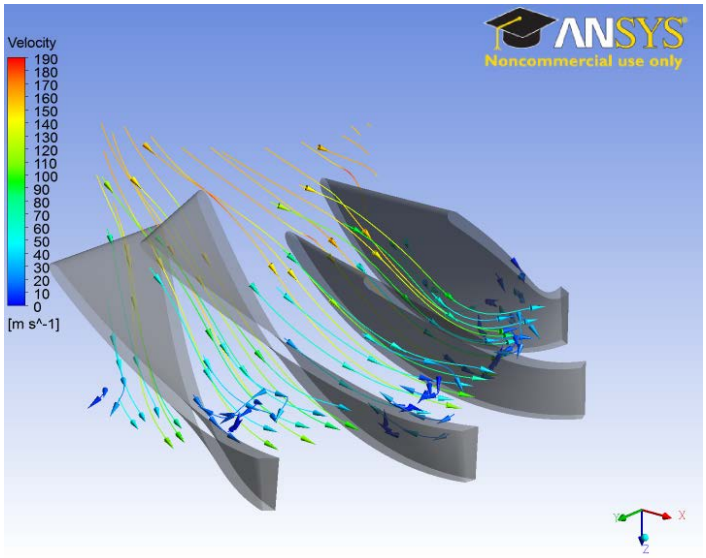

Figure 3.15: Velocity Streamline at Blade trailing edge

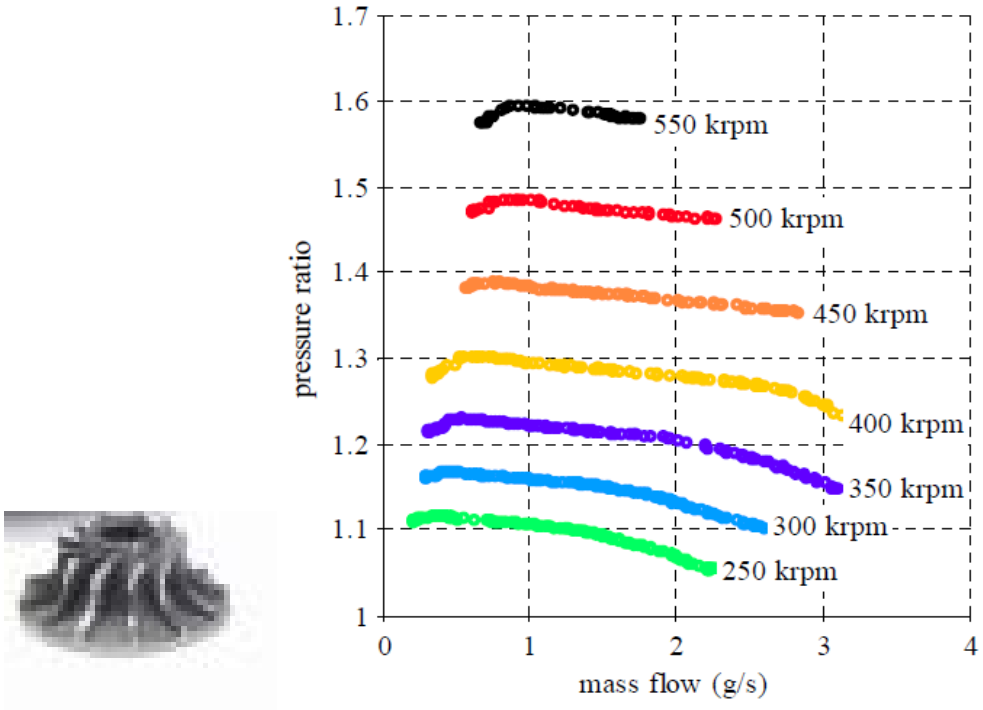

Figure 3.16: Performance map form the experimental results [3]

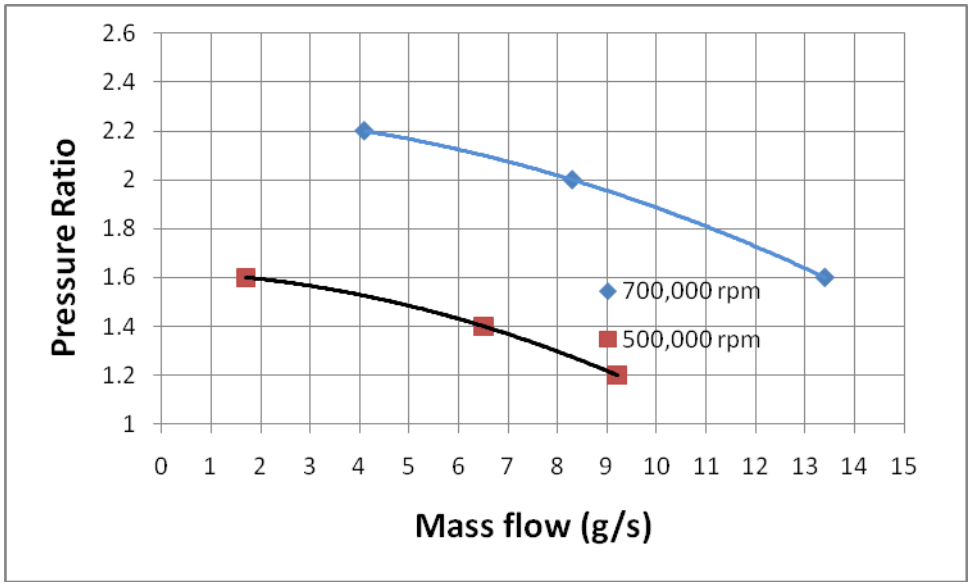

Figure 3.17: Compressor performance map (Number of Blades=10)

Simulation of the off-design performance of the centrifugal compressor stage was considered for three off design speeds (RPMs): 60%, 70%, 85% and 100% of design speed (700,000 rpm). Four different performance speed lines were constructed for these off-design operating conditions. These numerical predictions of the speed lines are compared directly to available experimental data. These results will be presented in this section.

The first performance measure investigated was the total to static pressure ratio. This is a ratio of the static pressure ratio at the exit divided by the total pressure at the inlet. In the Figure 3.17 and Figure 3.18 shows the plots of total to static pressure ratio as a function of the inlet and exit mass flow for blade number of 10. The plot of the pressure ratio as a function of mass flow is called the speed line. The plots clearly show the stall, operating and choke regions of the speed lines (Figure 3.18).

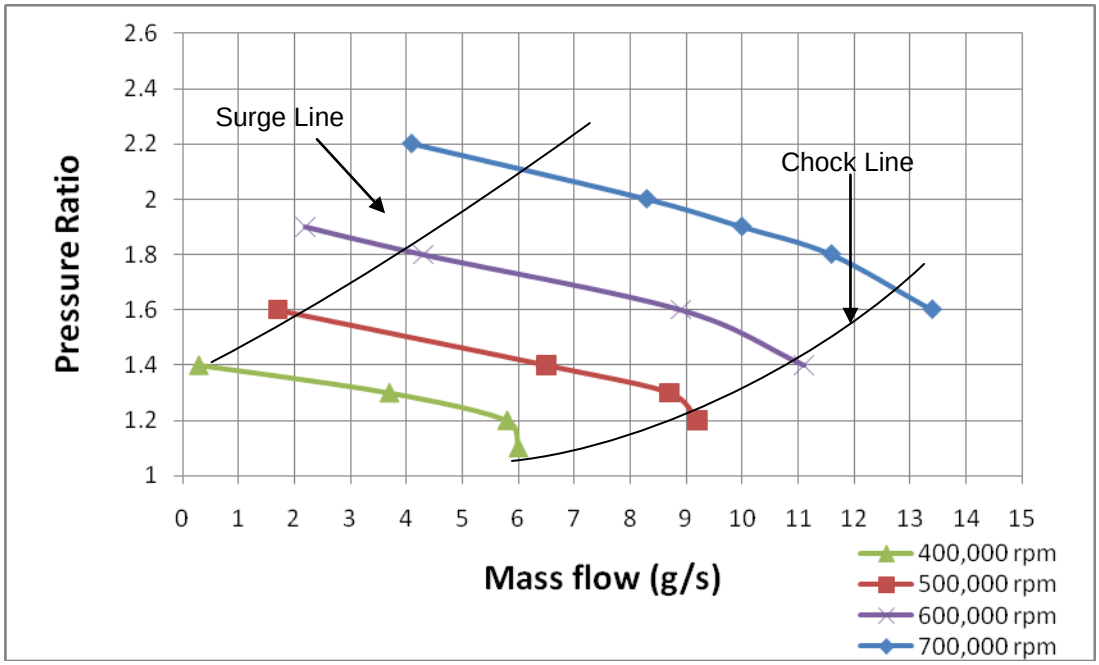

Figure 3.18: Compressor performance map

Because surge is an unsteady phenomenon that cannot be modeled with a steady state simulation, the convergence rate for the calculations tends to stall near surge. Although the results do not diverge, the solutions oscillate, which generates a high degree of error. Any decrease in mass flow rates after these points will result in greater and greater oscillations in the computed solution and the solution residual measures.

CHAPTER 4

EXPERIMENTAL SETUP FOR THE TURBOCOMPRESSOR SYSTEM

Whole system

A test rig was designed in the SolidWorks (Figure 4.1) to evaluate rotordynamics performance of the bearing as well as the compressor performance.

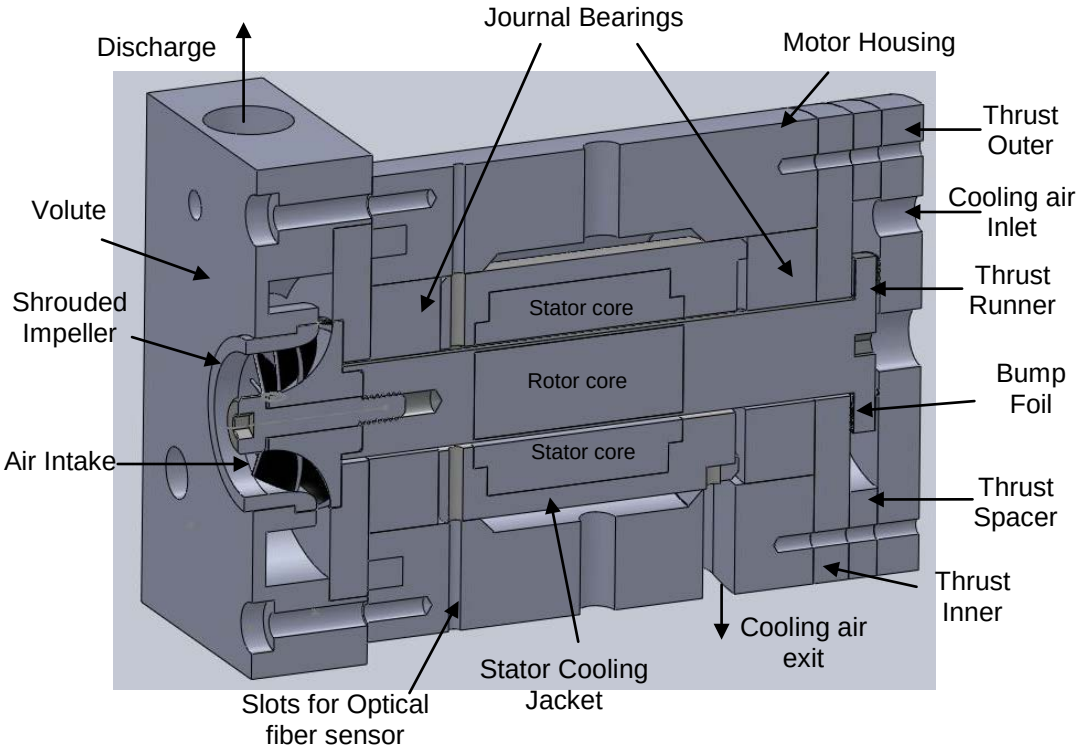

Figure 4.1: Motor Assembly with Impeller and Volute

Detail design of the components

Volute:

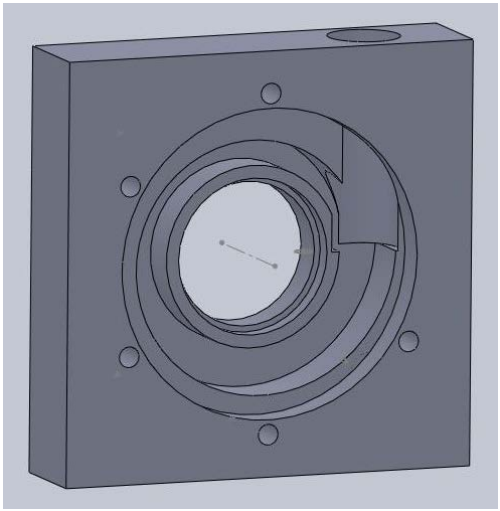

Figure 4.2: Volute

The purpose of the volute is to collect the pressurized air from the impeller and discharge through the specific application like inside the fuel cell or gas turbine engines.

Volute flange:

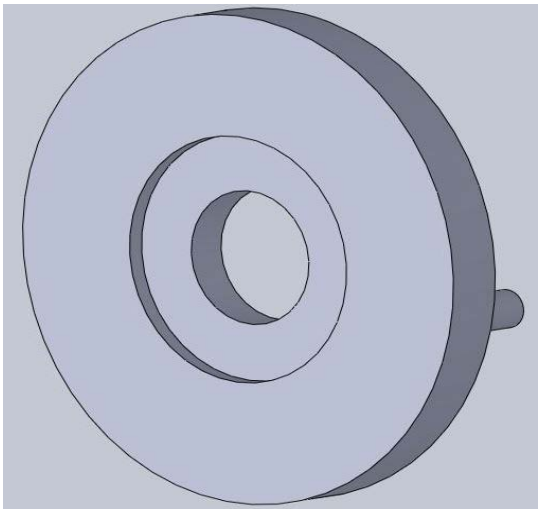

Figure 4.3: Volute flange

Compressor Impeller:

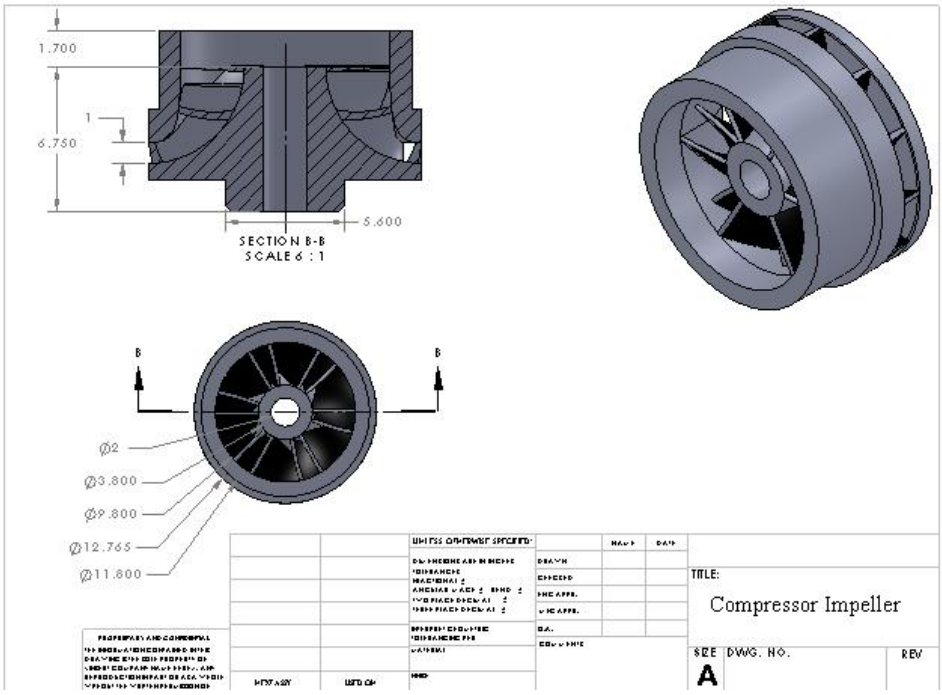

Figure 4.4: Compressor Impeller

The most important part in the test rig and its purpose is to pressurize the air to a certain pressure ratio and maintain a specific mass flow rate. The blade thickness was set 0.225mm according to the minimum thickness that the selective laser sintering process can do in precision machining about 0.00875inch (0.222mm).

Rotor:

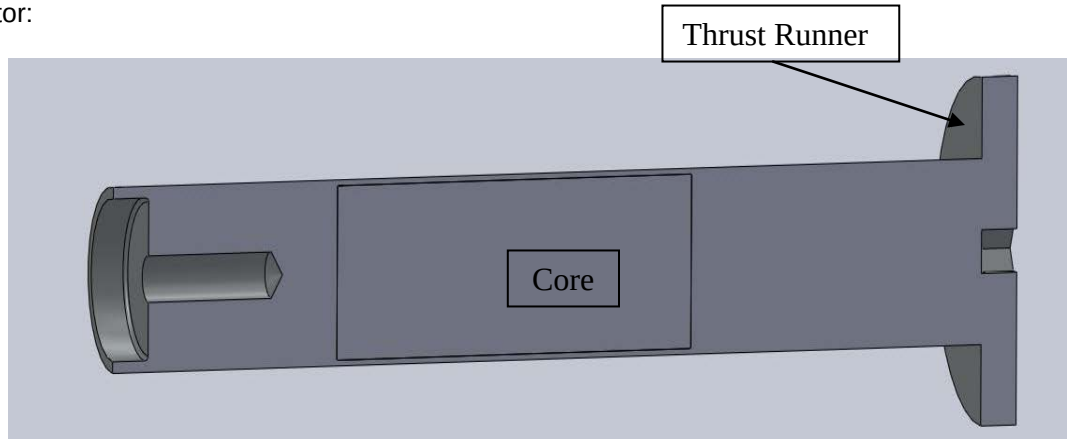

Figure 4.5: Rotor with core

Rotor spins in the magnetic field inside the stator at the targeted speed set from the controller.

Motor Housing:

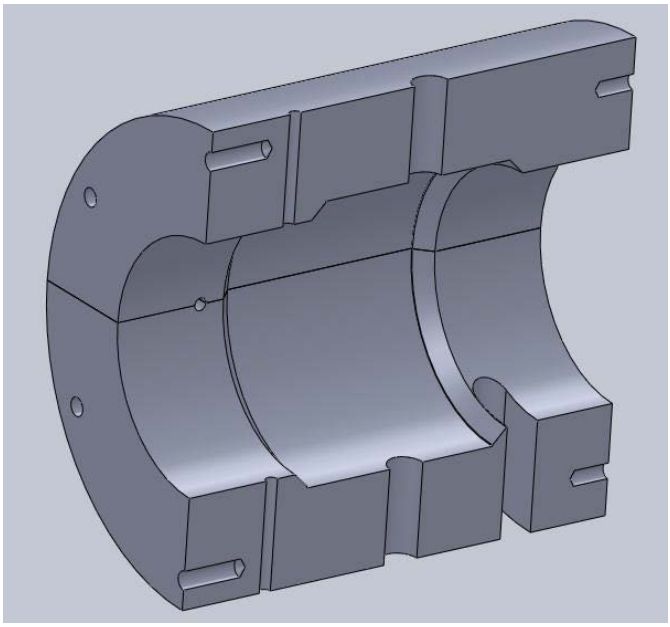

Figure 4.6: Cross section view of the motor housing

The motor Housing accommodates every components of the test rig and provides necessary support.

Journal Bearing:

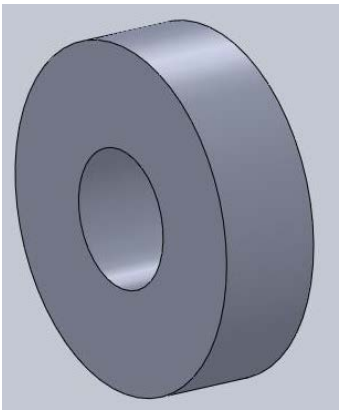

Figure 4.7: Journal Bearing (Foil bearing not shown)

One of the most important components which carry the total load of the shaft as well as the impeller and any disturbance form outside.

Stator with core:

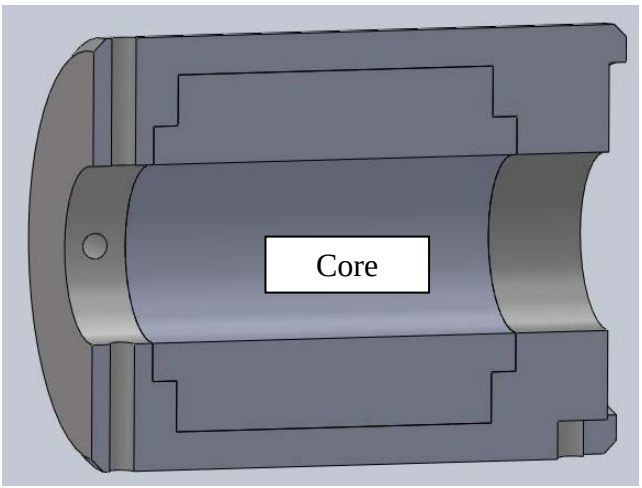

Figure 4.8: Stator

The main purpose of the stator is to provide necessary magnetic field to the rotor as assigned from the controller.

Celeroton Technology a company in Switzerland manufacture ultra high-speed electrical drive systems agreed to provide the high speed micro motor drive for the turbocompressor

system designed. They will provide stator, PM rotor, motor housing with necessary holes and tapes in the motor (Figure 4.1,Figure 4.5,Figure 4.6,Figure 4.8).

Thrust Bearings

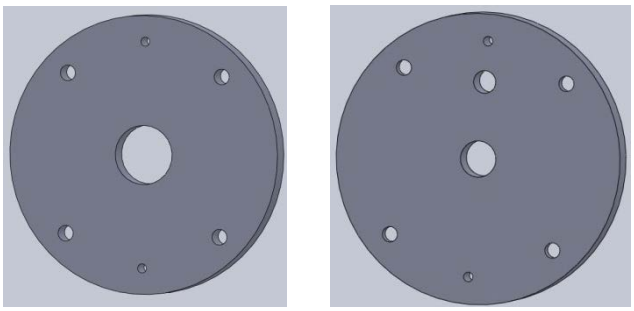

(a) (b)

Figure 4.9: Thrust Disk (a) Inner, (b) Outer

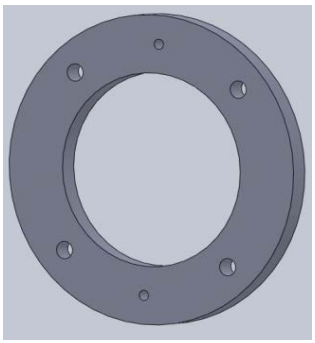

Figure 4.10: Thrust Spacer

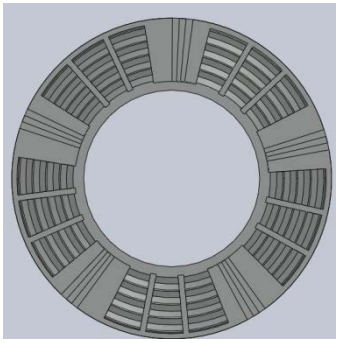

Figure 4.11: Bump Foil for Both the Thrust Disk

Sensors and Controllers:

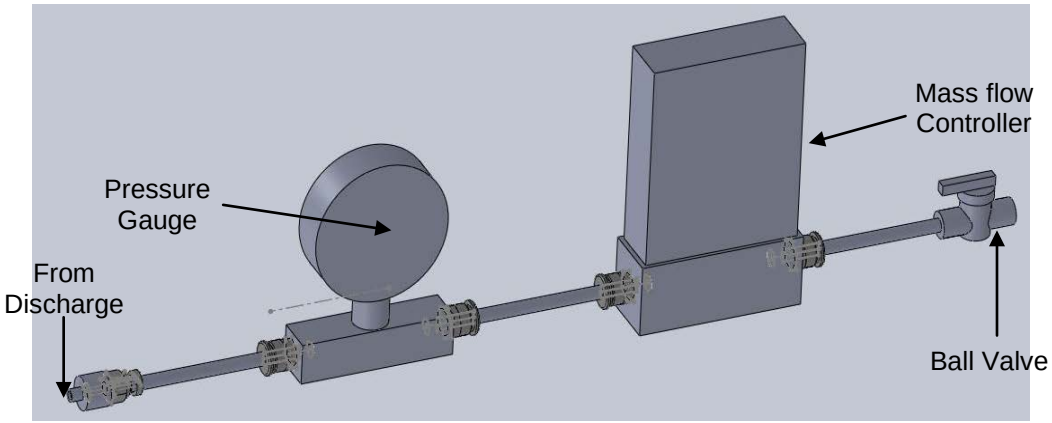

Figure 4.12: Mass flow Controller and Pressure Gauge

CHAPTER 5

CONCLUSIONS AND RECOMMENDATIONS

5.1. Conclusions

5.1.1. Bearing test

Spin tests were performed for threes type of Air Foil Bearing. For the first case dental drill air turbine drive were used for spinning up to 260,000 rpm. For second case (LIGA bearing elastic foundation) spin tests were performed up to 400,000 using Electric motor drive and results were shown up to 350,000 rpm. In the third rotorbearing test (corrugated bump foil bearing) spin were carried out up to 410,000 rpm and corresponding results are shown.

In First Rotordynamics test the vibration amplitude in the vertical was more than horizontal amplitude as the bearing was softer in horizontal direction. Due to non uniform tip clearance and strong aerodynamic force in the turbine impeller, some sub-synchronous vibrations were observed in ~50,000 rpm but disappear with the speed increase of the rotor. The spinning test in the second run was performed very smoothly. There were certain parameters that were very difficult to control at the time of test as 1) turbine shroud was installed without any direct maneuvering mechanism for both axial and transverse direction, 2) axis of air nozzle and the center plane of the turbine drive was not matched which results an unbalance in the rotor, 3) air nozzle in the thrust air pad did not provide a stable and uniform pressure from both side of rotor.

In second Rotordynamics test, similar type response considering the amplitude of the vibration except the amplitude slightly increased after ~200,000 rpm were observed. Hydrodynamic pressure developed inside the journal bearing during the high speed (350,000~400,000 rpm) reached at certain point that the top foil of the bearing came off and the motor was stopped.

In third Rotordynamics test both synchronous and sub-synchronous amplitude in both horizontal and vertical direction was observed higher than previous test (Test 1 & Test 2). Some external noise, uncertainty from the surface of the bearing or some unknown parameter may cause this high amplitude. The spinning tests were performed up to 410,000 rpm and very large subsynchronous vibration observed after ~360,000 rpm as bearing failure on that point is suspected

5.1.2.Simulation and design

The performance of a centrifugal compressor has been analyzed after modeling in BladeGen and TurboGrid, and using CFD software ANSYS ICEM CFD to generate high quality Structural meshes, CFX as the solver. With lower speed, entire speed map was generated with high accuracy particularly lower rotational velocities. Surge prediction is also an unsteady phenomenon which means it is an area that can be improved upon. Fully unsteady flow analyses can yield better performance predictions particularly at high rotational speeds.

5.2. Recommendations for future work

5.2.1.Bearing test:

For full LIGA bearing (second rotordynamics test) at very high speed over 350,000 the hydrodynamic pressure inside the bearing was so high that the top foil came off. Design modification for this bearing for securing the top foil can be done to avoid this kind of situation.

Thrust bearing clearance and thrust forces played a major role in imbalance response of a rotor bearing system. Thrust bearing assembly was one of the critical issues as it eventually maintained the clearance between the thrust disk and the thrust runner. Typical clearance should not more than 10 μm. It was the manufacturing limitation to have a very high accuracy uniform thickness at the time of manufacturing the thrust spacer. It was very difficult to maintain uniform air pressure developed inside the thrust spacer form both side of the thrust disk.

It was quit impossible to assemble the dummy impeller and the shaft at the point of balancing. Dowel pin assembly would be a better solution to reduce this complexity.

5.2.2.Simulations and design:

Mesh size (both number of elements and number of nodes) can be increased to have more accurate results.

Unsteady flow analysis can be done to have better understanding of the performance of compressor.

After getting some experimental data for the turbocompressor system designed, some more iteration of the simulation in both design and off design cases can be done using the corrected boundary condition from experiments.

Volute geometry can be included as stator/rotor approach in the numerical simulation process to have the total performance of the compressor..

Design optimization for both compressor blade and volute can be done to full fill the required flow performance i.e. mass flow, pressure ratio etc.

APPENDIX A

SETUP AND OPERATION OF SPIN TEST RIG

The section outlines the procedure and instructions for setting up the test rig and also its operation. Also discussed in detail is the procedure to assemble the bearing, alignment of the bearing with rotor, hardware connections and calibration of fiber optic probes.

Bearing Setup and Alignment:

As shown in the Figure A.1 (a), when install the journal bearing in the bearing housing of the motor rotational direction and orientation of the bearing should be taken care of. Two journal bearings with 90° off set has to set in the impeller side of the motor, Two journal bearings has to set inside the rear cover of the motor as same back to back (90° off set) configuration.

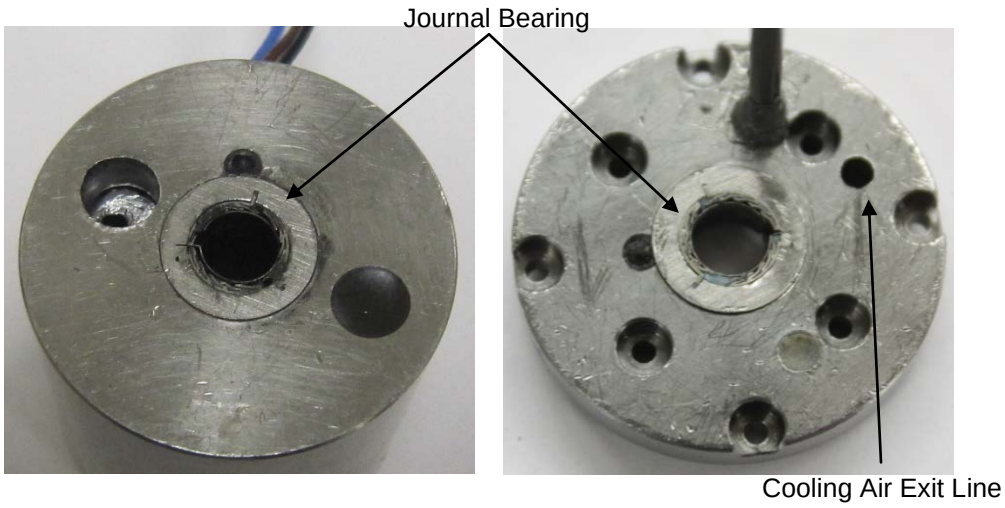

Figure A.1: Bearing installation inside the bearing housing of the motor, (a) Impeller side, (b) Motor Cover side

To ensure uniform air pressure from both side of the thrust bearing (hydrostatic) the high pressure cooling air line should go through the small holes of the both thrust disk to ambient condition. So for this, one cooling line inside the stator should blocked by epoxy on the line of the cooling air intake Figure A.1.

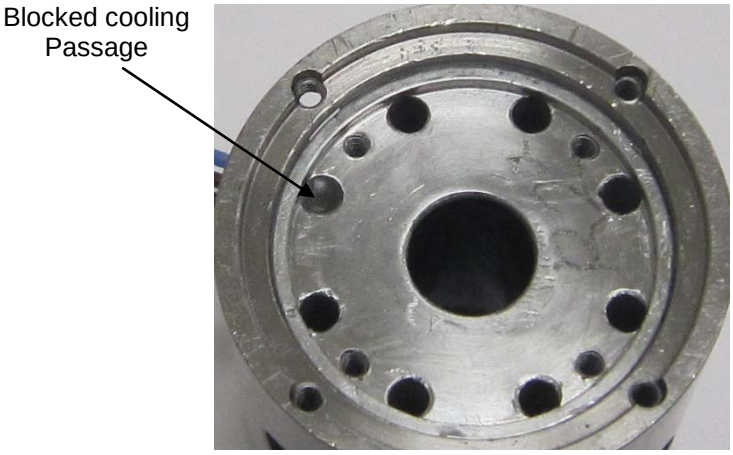

Figure A.2: Blocked cooling line inside the stator

Stator of the motor should put inside the stator housing ensuring the alignment of cooling air line. Then set the inner thrust bearing inside the stator and then insert the PM rotor inside the stator very carefully because the rotor surface may cause damage to the top foil of the journal bearing. Rotor and dummy impeller are aligned along with the mark of the rotor and impeller as it is quit tricky to tighten the left hand screw (Figure A.3 (a) and (b)).

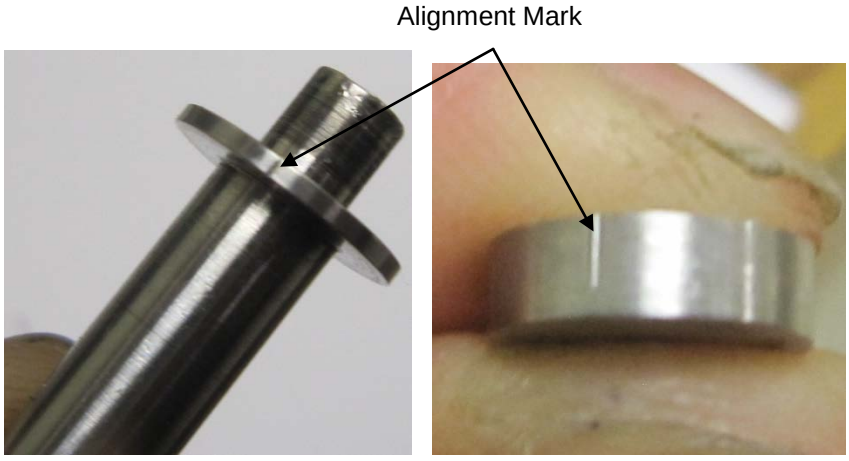

Figure A.3: Alignment mark in the (a) Rotor and in the (b) Dummy impeller

The thrust spacer then set inside the motor and at the same time set the outer thrust disk inside the outer cover of the motor. Then attach the outer cover of the motor with the motor

housing. Four screws are attached with the stator and the outer cover to ensure the thrust clearance exactly the same as spacer.

Two fiber optic probes are installed inside the Pedestal of the Motor as one is in Horizontal direction and other is in the vertical direction. The tip of the probe should set in their linear range (discussed later).

Spin Test:

After assemble all the components to the motor and motor housing motor power cable is connected with the motor controller, controller is powered with a DC power supply up to 80V. 24 V DC supply is connected to the amplifier of the fiber optic probe. Using the Celeroton pilot comptroller software, motor start, stop and speed control is done. First press the start button on the controller software (Figure A.4) Without connected the motor cable to the controller to reset the port. Then connect the power cable of the motor to run the spin test for various speed.

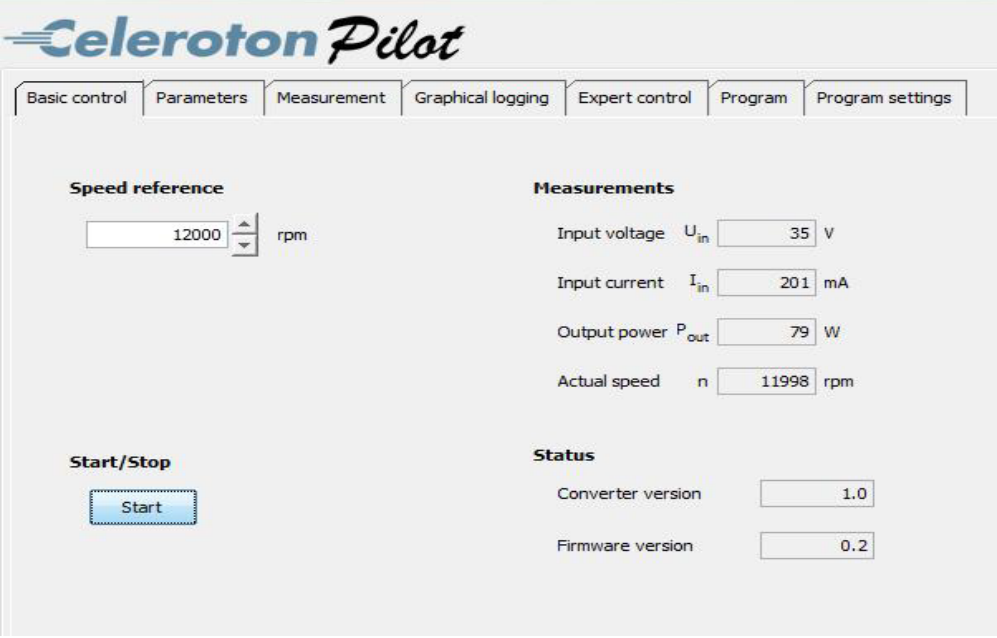

Figure A.4: Front panel view of the Celeroton Pilot Controller software

APPENDIX B

DESCRIPTION OF DIGITAL DATA ACQUISITION AND HARDWARE USED

The description of the data acquisition system (Figure B.1) setup was adopted from [24]. The equipments numbered in the figure are elaborated as

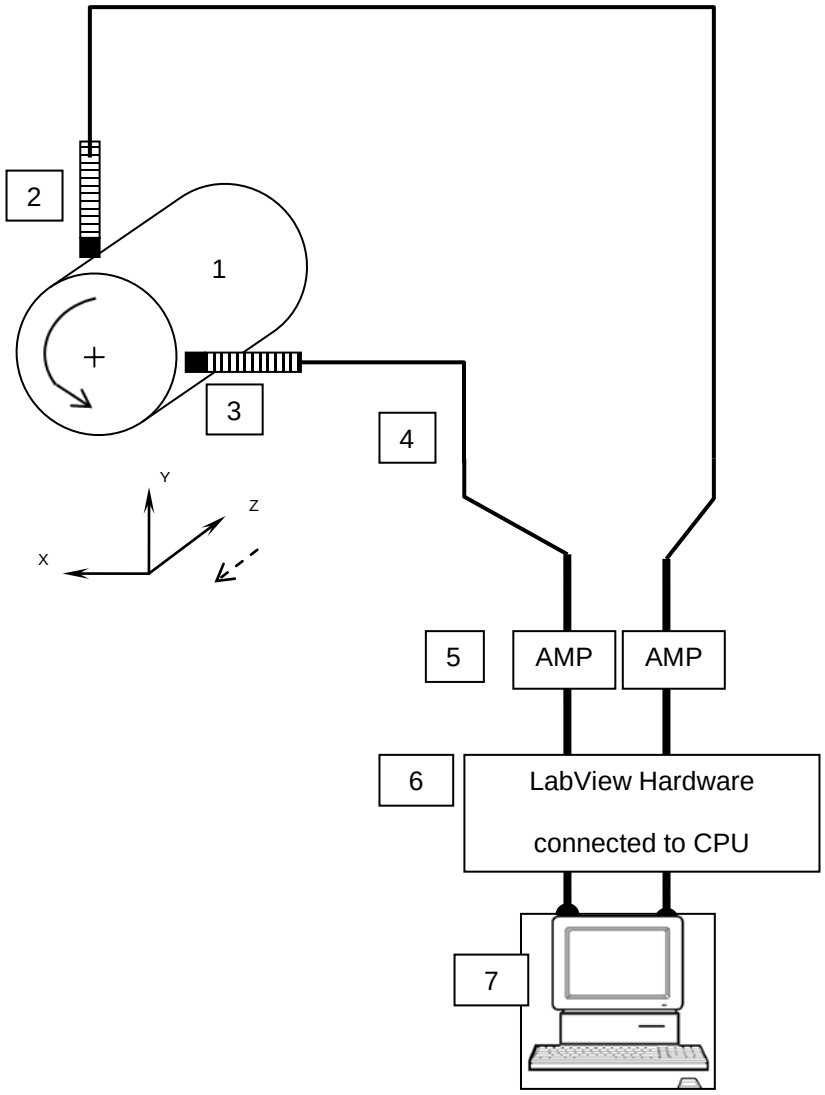

Figure B.1: Schematic of the components used for Data acquisition

Fiber Optic Probe wiring and calibration description:

The proximity probes used to measure the vibration signal are connected to the CPU amplifier. The wiring description is shown in Figure B.2. Once the connections are made, the probes are calibrated so that they are set up in the bearing housing at their linear range. The calibration details are presented in this section later.

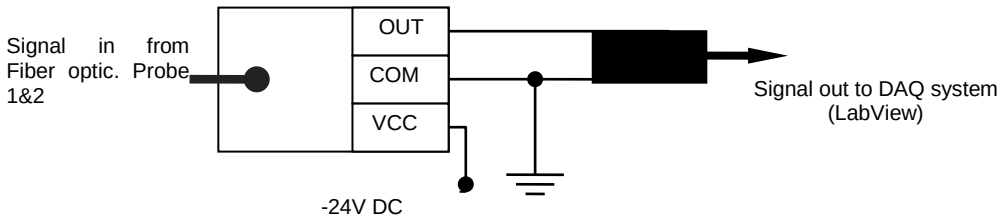

Figure B.2: Probe to Amplifier and then CPU

The probes are connected to the CPU LabView Hardware through an amplifier (Figure B.3). Once connected, the probes are calibrated with the rotor in position to obtain the linear range of the respective Fiber Optic probe. The Fiber Optic probes are mounted on a two axis linear stage Figure B.3. The probe is made to touch the rotor using the micrometer. This distance corresponds to distance 0 and the voltage corresponding to this distance is measures. Distance between the rotor and probe is varied using the micrometer and corresponding voltage readings are measured. The voltages are measured over a wide range up to 60 μm. The gain of the probe is measured from the straight line equation as taking the inverse of the tangent by using a simple two axis linear stage and is fed into the National Instruments LABVIEW 8.2 software. Details of the calibration results are shown in Figure B.4, Figure B.5 and Table B.1.

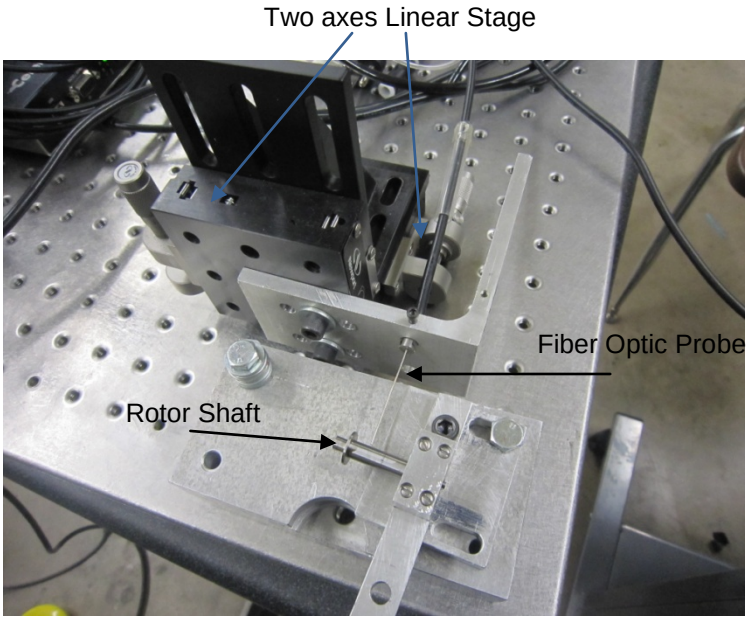

Figure B.3: Calibration of the Fiber Optic probe using two axis linear stages

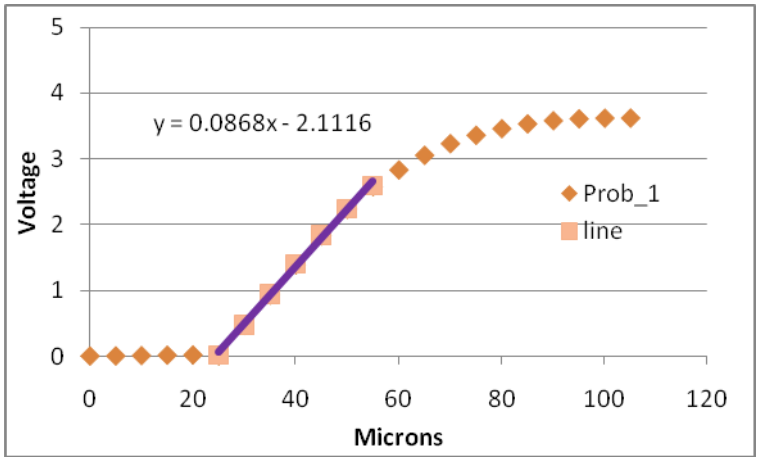

Figure B.4: Probe 1 calibration curve

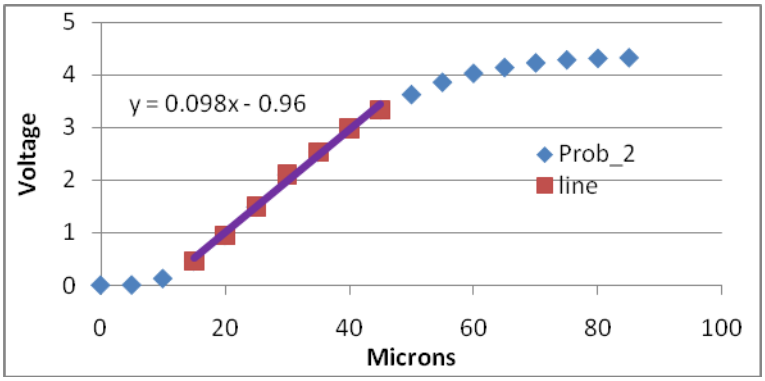

Figure B.5: Probe 2 calibration curve

Table B.1: Linear Range Fiber Optic Probe Calibration Data

Voltage (Volts) Probe 1	Voltage (Volts) Probe 2	Distance from Rotor (Microns)	Micro-Meter reading (Microns)
0.0265	0.4633	15	6.300
0.03	0.9505	20	6.305
0.01656	1.49	25	6.310
0.48	2.103	30	6.315
0.94	2.53	35	6.320
1.4	2.98	40	6.325
1.84	3.3351	45	6.330
2.244	3.6221	50	6.335
2.589	3.8538	55	6.340

The front panel of the LABVIEW rotordynamics software is as shown in Figure B.6.

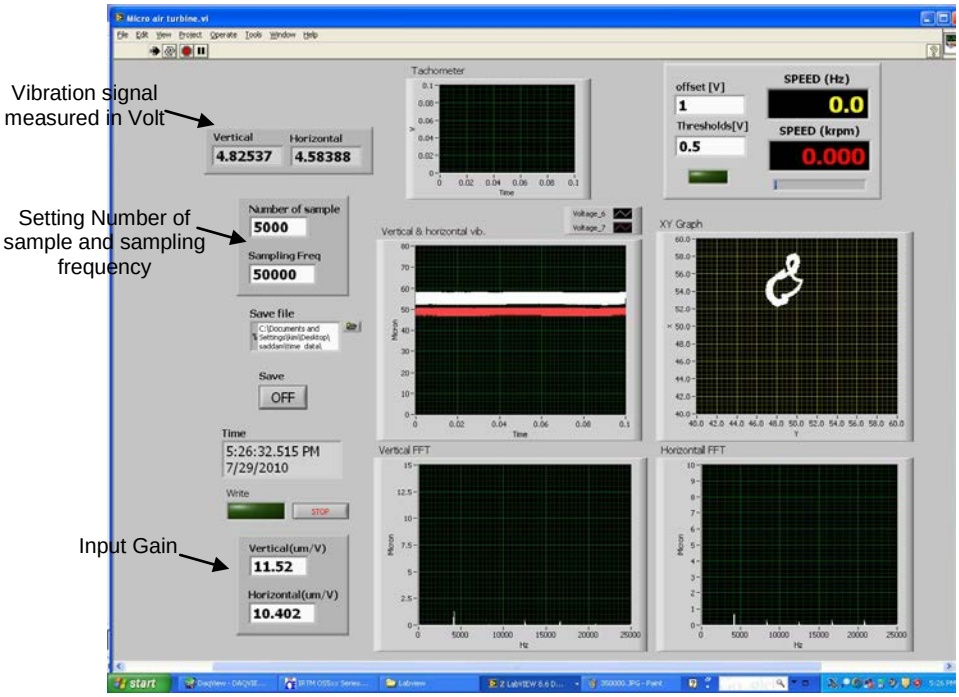

Figure B.6: Front Panel view of Labview Data Acquisition system running at 250,000 RPM

First set the sampling frequency and number of sample. As for example rotor running at ~400,000 rpm the minimum number of sample should be ~7000 (400,000/60) and sampling frequency should be more than or equal to the two times number of sample. From the calibration of the fiber optic probe we fed the gain to the LabView Window. When steady state happened we save a certain number vibration data for further use in the Matlab code to get the water fall plot.

APPENDIX C

PROCESS FOR MESH GENERATION IN ICEM CFD

The ANSYS ICEM CFD hexahedral mesh generator is an object-based, semi-automatic, multi-block structured or unstructured, surface and volume mesh generator. The block technique model is generated directly on, but independent of, the underlying CAD geometry. It is recognized as one of the fastest commercially available hexahedral mesh generation tools. ANSYS ICEM-CFD is projection based in that the surfaces of the mesh are automatically projected on to the nearest CAD surface. It is also possible to specify the projection of points, edges and surfaces for a greater degree of control. The steps towards the ultimate structured mesh generation process followed in this thesis are described below.

1. Export the *.tin format geometry file from TurboGrid to the ICEM-CFD Graphics User Interface as to open a new project.
2. Doing some editing in the surface and lines of the imported geometry file to make it compatible to the ICEM format for mesh generation. Editing process contain creating points in every line intersect; deleting unnecessary lines, points and surfaces. Fixing any geometry flaws occurring at the time of export from TurboGrid.
3. Defining every surface for the boundary condition as inlet, outlet, periodic, main blade, splitter blade, hub and shroud.
4. First generate surface mesh in the hub and shroud then extrude it to make volume mesh.

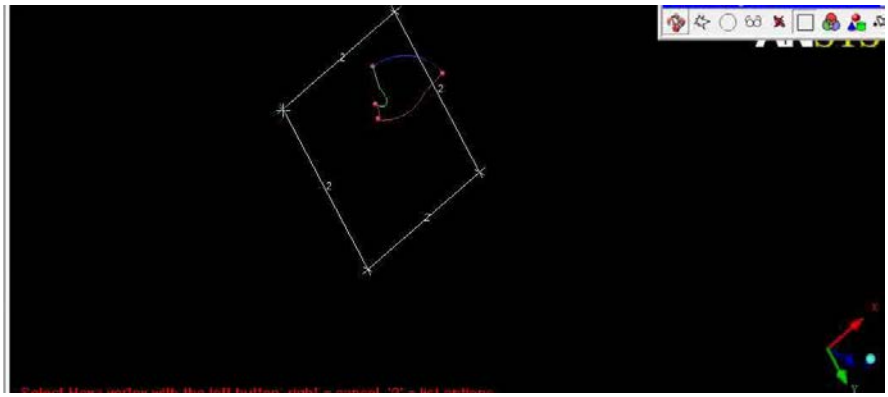

Figure C.1: Block above the hub surface

5. The blocking process initiates by drawing a 2D squire block above the surface of the hub (Figure C.1) on the side of shroud. Now associate each line and points to the corresponding line and points on the hub surface (Figure C.2).

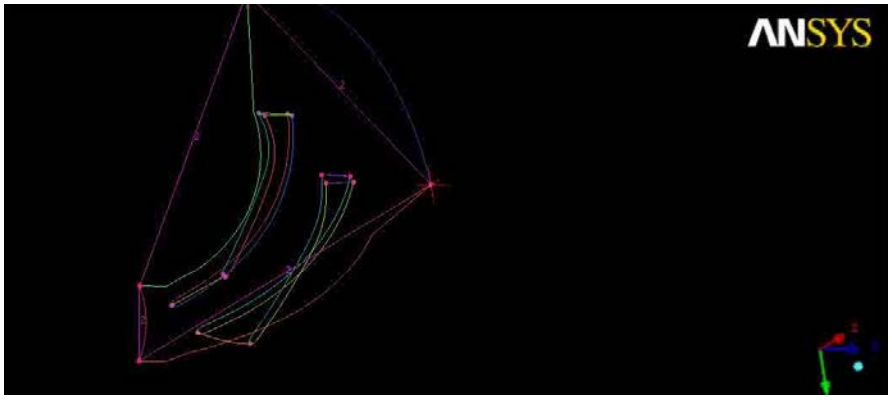

Figure C.2: Association of the line and points on the hub surface

6. Now divide the line on each side as necessary both in the inlet & Outlet and in the periodic side (Figure C.3).

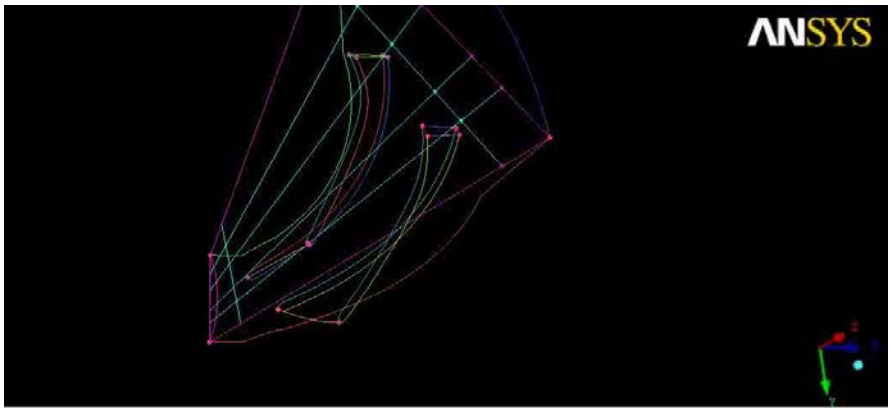

Figure C.3: Divided lines on each side of the block

7. Associate the divided lines, points to the corresponding lines and points on the blade and hub intersection surface (Figure C.4).

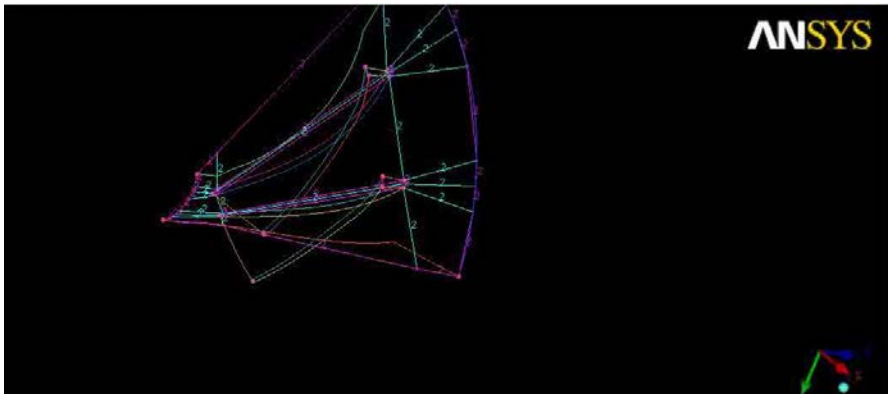

Figure C.4: Associated lines and points to the corresponding lines on the hub

8. After successful association on the hub divide each line along the flow direction to several sections as to create the surface mesh (Figure C.5). The number of divided section will eventually represent how fine the mesh is.

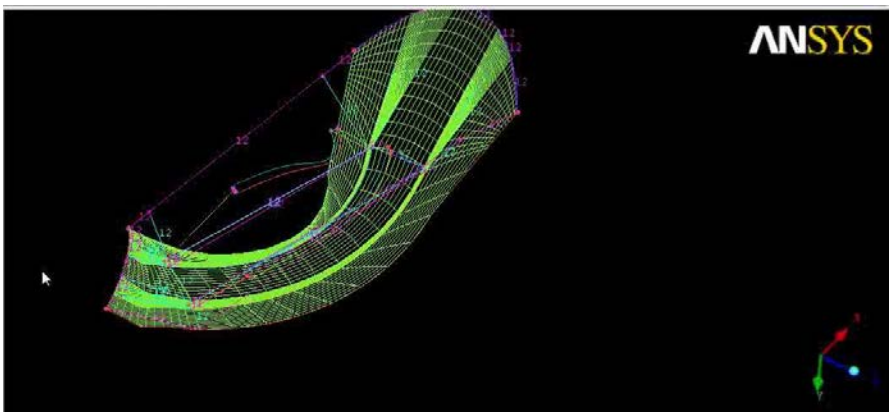

Figure C.5: Surface mesh on Hub

9. Extrude this towards the shroud for generate surface mesh on shroud surface and follow the same association, projection and divide process (Figure C.6).

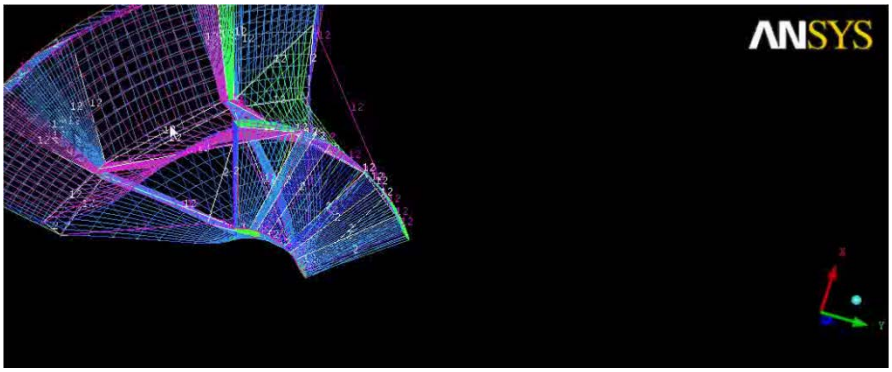

Figure C.6: Surface mesh on both hub and shroud

10. Now convert 2D surface mesh to 3D volume mesh and we also can increase the number of elements by dividing the block line along the edge of the geometry (Figure C.7).

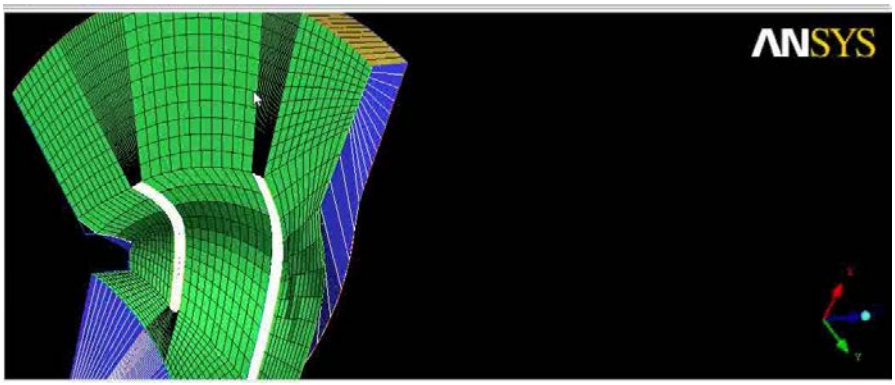

Figure C.7: Volume form 2D surface mesh

11. After creating the volume mesh we delete the block created inside the blades as we do not want to create mesh inside the blades.
12. Finally we check the quality of the mesh (Figure C.8 & Figure C.9)and any flaws occurring at the time of mesh generation. We check the different quality parameter values whether they maintain the required level in the mesh i.e. presence of negative volume, minimum volume (should be below 0.3), maximum volume ratio between the elements, minimum & maximum angle, etc. If any of these problem found in the mesh

then fixed with appropriate way, by changing the orientations of blocks, line, edge and points to meet the required level.

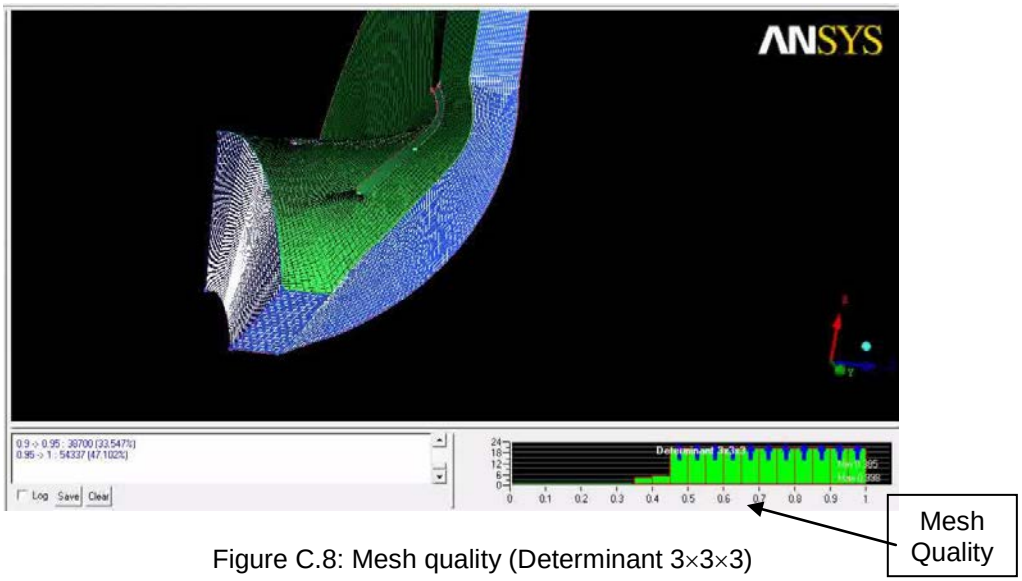

Figure C.8: Mesh quality (Determinant 3×3×3)

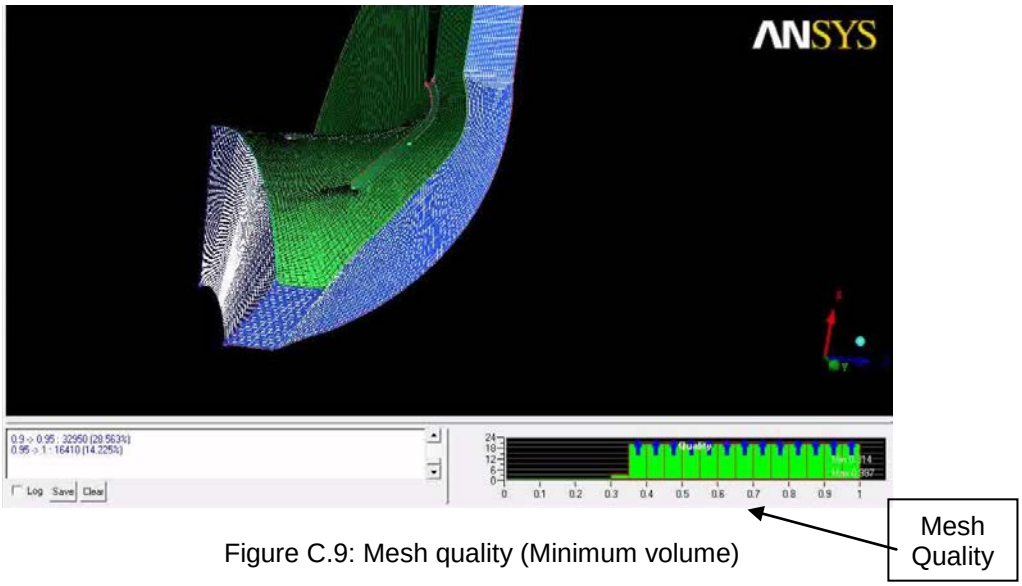

Figure C.9: Mesh quality (Minimum volume)

13. When every flaws and problems are solved then convert the structure mesh to unstructured mesh as CFX uses Finite Volume Method and it can only handle unstructured mesh. Save the mesh as the format of cfx5 to use further in CFX solver.

,

BIBLIOGRAPHY

[1] Kim, D., Creary, A., Chang, S. S., and Kim, J. H., 2009, "Meso-Scale Foil Gas Bearings for Palm-Sized Turbomachinery: Design, Manufacturing, and Modeling," Journal of Engineering for Gas Turbines and Power**, 131**(2), pp. 042502 (10 pages).

[2] Kim, D., Rimpel, A. M., Chang, S. S., and Kim, J. H., 2009, "Design and Manufacturing of Meso Scale Tilting Pad Gas Bearings for 100-200W Class PowerMEMS Applications," Journal of Engineering for Gas Turbines and Power**, 131**(3), pp. 042503.1-042503.11.

[3] Krähenbühl, D., Zwyssig, C., Wese, H., and Kolar, J., 2008, "A Miniature Turbocompressor System," Proceedings of the Smart Energy Strategies, Zurich, Switzerland.

[4] Agrawal, G. L., 1997, "Foil Air/Gas Bearing Technology -- an Overview," International Gas Turbine & Aeroengine Congress & Exhibition, Orlando, FL, ASME Paper No. 97-GT-347.

[5] Heshmat, H., and Roger Ku, C., 1992, "Compliant Foil Bearing Structural Stiffness Analysis: Part I—Theoretical Model Including Strip and Variable Bump Foil Geometry," Journal of Tribology, **114**(2), pp. 394-401.

[6] Heshmat, H., 1994, "Advancements in the Performance of Aerodynamic Foil Journal," Journal of Tribology, **116**(2), pp. 287-294.

[7] Rubio, D., and Andrés, L., 2006, "Bump-Type Foil Bearing Structural Stiffness: Experiments and Predictions," Journal of Engineering for Gas Turbines and Power**, 128**(3), pp. 653.

[8] Hikichi, K., Togo, S., Isomura, K., Saji, N., Esashi, M., and Tanaka, S., 2009, "ULTRA-HIGH-SPEED TAPE-TYPE RADIAL FOIL BEARING FOR MICRO TURBOMACHINERY," Proceedings Power MEMS, Washington DC.

[9] Kim, D., and Creary, A., 2008, "
LIGA-Fabricated Meso Scale Foil Gas Bearings for Palm-Sized Microturbomachinery," **ASME Conference Proceedings**, Miami, Florida, October 20–22, 2008.

[10] Zwyssig, C., Kolar, J. W., and Round, S. D., 2009, "Megaspeed Drive Systems: Pushing Beyond 1 Million rev/min," Mechatronics, IEEE/ASME Transactions on**, 14**(5), pp. 564-574.

[11] Zwyssig, C., and Kolar, J., 2006, "Design Considerations and Experimental Results of a 100 W, 500 000 Rpm Electrical Generator," Journal of Micromechanics and Microengineering, **16**(9).

[12] Krähenbühl, D., Zwyssig, C., Wese, H., and Kolar, J., 2009, "Theoretical and Experimental Results of a Mesoscale Electric Power Generation System from Pressurized Gas Flow," Journal of Micromechanics and Microengineering, **19**(9).

[13] Krähenbühl, D., Zwyssig, C., Weser, H., and Kolar, j., 2010, "A Miniature 500 000-r/min Electrically Driven Turbocompressor," IEEE TRANSACTIONS ON INDUSTRY APPLICATIONS**, 46**(6).

[14] Epstein, A., 2003, "Millimeter-Scale, MEMS Gas Turbine Engines," ASME Turbo Expo 2003, Atlanta, Georgia, 16-19, 2003.

[15] Epstein, A., 2004, "Millimeter-Scale, Micro-Electro-Mechanical Systems Gas Turbine Engines," Journal of Engineering for Gas Turbines and Power**, 126**(2), pp. 205.

[16] Aghaei tog, R., Tousi, A., and Soltani, M., 2007, "Design and CFD Analysis of Centrifugal Compressor for a Microgasturbine," Aircraft Engineering and Aerospace Technology**, 79**(2), pp. 137-143.

[17] Saaresti, T., Reunanen, A., and Larjola, J., 2006, "Computational and Experimental Study of Pinch on the Performance of a Vaneless Diffuser in a Centrifugal Compressor," Journal of Thermal Science**, 15**(4), pp. 306-313.

[18] Jiaoa, K., Sunb, H., Lia, X., Wua, H., Krivitzkyc, E., Schramb, T., and Larosilierec, L., 2009, "Numerical Simulation of Air Flow through Turbocharger Compressors with Dual Volute Design," Applied Energy**, 88**(9), pp. 2494-2506.

[19] Xiao, J., Gu, C., Shu, X., and Gao, C., 2006, "Performance Analysis of a Centrifugal Compressor with Variable Inlet Guide Vanes," FRONTIERS OF ENERGY AND POWER ENGINEERING IN CHINA**, 1**(4), pp. 473-476.

[20] Krähenbühl, D., Zwyssig, C., Hörler, H., and Kolar, J. W., 2008, "Design Considerations and Experimental Results of a 60 W Compressed-Air-to-Electric-Power System," 2008 IEEE/ASME International Conference on Mechatronic and Embedded Systems and Applications, Beijing, China, October 12-15.

[21] Schoberiri, M., 2005, *Turbomachinery Flow Physics and Dynamic Performance*, Springer, USA, pp. 522.

[22] Ki, J., and Kim, D., 2010, "Computational Model to Predict Thermal Dynamics of Planar Solid Oxide Fuel Cell Stack during Start-Up Process," Journal of Power Sources**, 195**, pp. 3186-3200.

[23] Wilcox, D.C., 1993, *Turbulance Modeling for CFD*, DCW Industries, CANADA, pp. 477.

[24] Rimpel, A., and Kim, D., 2009, "Experimental and Analytical Studies on Flexure Pivot Tilting Pad Gas Bearings with Dampers Applied to Radially Compliant Pads," ASME Journal of Tribology**, 131**(3), pp. 041001 (10 pages).

BIOGRAPHICAL INFORMATION

MD SADDAM HOSSAIN received his Bachelor of Science degree in Mechanical Engineering from Bangladesh University of Engineering and Technology, Bangladesh, in January 2008. He is currently pursuing his Master of Sciences degree in Mechanical Engineering at The University of Texas at Arlington, USA. He is a member of the Microturbomachinery and energy Systems Lab, guided by Daejong Kim. His research interests include CFD, Rotordynamics, Finite Element Method, Control Systems and design and fabrication with emphasis on SolidWorks, Ansys, Pro/E, and Unigraphics.